1   **Running head:**

2   Image-based plant disease phenotyping

3

4   **Author to whom all correspondence should be sent:**

5   Rebecca Bart

6   Donald Danforth Plant Science Center

7   975 North Warson Road

8   Saint Louis, MO 63132

9   Tel: 314-587-1696

10   Email: rbart@danforthcenter.org

11

12   **Research area:**

13   Ecophysiology and Sustainability

14

15

16

17

18

19

20

21

22

23

24

25

26

27

28

29

30

31

32 **Quantitative, image-based phenotyping methods provide insight into spatial and**

33 **temporal dimensions of plant disease**

34

35 Andrew M. Mutka[a], Sarah J. Fentress[a], Joel W. Sher[a], Jeffrey C. Berry[a], Chelsea Pretz[a],

36 Dmitri A. Nusinow[a] and Rebecca Bart[ab]

37

38 [a]Donald Danforth Plant Science Center, Saint Louis, MO

39

40 **Summary:**

41 Novel, image-based phenotyping methods enhance characterization of plant-pathogen

42 interactions.

43

44

45

46

47

48

49

50

51

52

53

54

55

56

57

58

59

60

61

62

63 **Footnotes:**

64 **Author contributions**

65 A.M.M. designed and performed experiments, analyzed data, and co-wrote the paper.

66 S.J.F. created bioluminescent bacterial strains, performed experiments, and edited the

67 paper. J.W.S. and C.P. performed experiments and provided technical assistance. J.C.B.

68 performed statistical analyses. D.A.N. co-supervised the development of the

69 bioluminescent imaging techniques and edited the paper. R.B. designed experiments,

70 supervised the study, and co-wrote the paper.

71

72 **Financial sources**

73 This work was supported by the Donald Danforth Plant Science Center.

74

75 [b]**Corresponding author: Rebecca Bart**

76 Email: rbart@danforthcenter.org

77

78

79

80

81

82

83

84

85

86

87

88

89

90

91

92

93

94 **Abstract**

95 Plant disease symptoms exhibit complex spatial and temporal patterns that are

96 challenging to quantify. Image-based phenotyping approaches enable multi-dimensional

97 characterization of host-microbe interactions and are well suited to capture spatial and

98 temporal data that are key to understanding disease progression. We applied image-based

99 methods to investigate cassava bacterial blight, which is caused by the pathogen

100 *Xanthomonas axonopodis* pv. *manihotis* (*Xam*). We generated *Xam* strains in which

101 individual predicted type III effector (T3E) genes were mutated and applied multiple

102 imaging approaches to investigate the role of these proteins in bacterial virulence.

103 Specifically, we quantified bacterial populations, water-soaking disease symptoms, and

104 pathogen spread from the site of inoculation over time for strains with mutations in

105 *avrBs2*, *xopX*, and *xopK* as compared to wild-type *Xam*. Δ*avrBs2* and Δ*xopX* both

106 showed reduced growth *in planta* and delayed spread through the vasculature system of

107 cassava. Δ*avrBs2* exhibited reduced water-soaking symptoms at the site of inoculation. In

108 contrast, Δ*xopK* exhibited enhanced induction of disease symptoms at the site of

109 inoculation but reduced spread through the vasculature. Our results highlight the

110 importance of adopting a multi-pronged approach to plant disease phenotyping to more

111 fully understand the roles of T3Es in virulence. Finally, we demonstrate that the

112 approaches used in this study can be extended to many host-microbe systems and

113 increase the dimensions of phenotype that can be explored.

114

115

116

117

118

119

120

121

122

123

124

4

125

Introduction

126

127   Plant diseases are responsible for significant reductions in agricultural
128 productivity worldwide, and for many diseases, control strategies are not available
129 (Chakraborty and Newton, 2011). Elucidating the molecular mechanisms that govern
130 host-microbe interactions has a robust track record of leading to the development of new
131 and effective resistance strategies. For example, plant innate immunity employs several
132 tiers of receptors that, at least in some instances, can be transferred among species (Tai et
133 al., 1999; Zhao et al., 2005; Lacombe et al., 2010; Tripathi et al., 2014; Schoonbeek et al.,
134 2015). Similarly, molecular dissection of the mechanisms used by pathogens to induce
135 susceptibility has led to the development of biotechnology methods for blocking
136 pathogenesis (Li et al., 2012; Strauß et al., 2012; Boch et al., 2014). A more complete
137 understanding of the mechanisms used by plant pathogens to cause disease is likely to
138 lead to the development of additional strategies with potential for translation to the field.

139   Collectively, research conducted over the past few decades has revealed a
140 complicated web of crosstalk that forms our current multi-tiered model of plant-pathogen
141 interactions. Plant pattern recognition receptors (PRRs) initiate immune responses after
142 recognition of conserved microbial features, such as flagellin and EF-Tu for bacteria and
143 chitin for fungi (Macho and Zipfel, 2014). Successful pathogens have evolved effector
144 proteins to suppress defenses and induce susceptibility within their hosts (Win et al.,
145 2012). Resistant hosts may recognize these effectors or their action to trigger robust
146 immune responses (Stam et al., 2014; Khan et al., 2016). Type III effectors (T3Es)
147 secreted into host cells by Gram-negative bacteria are among the most intensely studied
148 pathogen effector proteins, and yet, the function of most T3Es remains unknown.
149 Members of the *Xanthomonas* and *Pseudomonas* genera are among the most common
150 bacterial disease-causing agents and are known to have large and variable effector
151 repertoires (White et al., 2009; Lindeberg et al., 2012; Schornack et al., 2013). Efforts to
152 deduce the role of individual T3Es in bacterial virulence through characterization of
153 effector knockouts have concluded that while collectively important, many individual
154 effectors do not contribute substantially to virulence (Castañeda et al., 2005; Kvitko et
155 al., 2009; Cunnac et al., 2011; Dunger et al., 2012; Xie et al., 2012).

156   Advances in DNA sequencing technologies have provided a wealth of genomic
157   resources for bacterial species. Using genomics data generated from pathogenic bacteria,
158   we are able to predict T3E repertoires, and the function of individual effectors can then
159   be investigated with genetic knockouts (Baltrus et al., 2011; Bart et al., 2012; Roux et al.,
160   2015; Wei et al., 2015; Teper et al., 2016). Traditional plant disease phenotyping methods
161   have relied on visual assessment of symptoms (Bock et al., 2010) and quantification of
162   pathogen growth in host tissue (Whalen et al., 1991; Tornero and Dangl, 2001; Liu et al.,
163   2015). Visual inspection and scoring of symptoms are likely to be translatable to disease
164   progression within field settings. Inspection and scoring, however, are subject to surveyor
165   bias and may not capture subtle differences in disease severity (Poland and Nelson,
166   2011). Quantification of pathogen growth is a tractable system for comparison, but fails
167   to provide information regarding the complex spatial patterns of diseases that progress
168   over time. Thus, genetic studies of T3E mutants have likely missed phenotypes that are
169   difficult to measure with traditional methods, and new approaches are needed for
170   exploring additional dimensions of disease phenotypes.

171   High-throughput, image-based phenotyping methods are revolutionizing many
172   areas of plant biology research (Furbank and Tester, 2011; Fiorani and Schurr, 2013;
173   Araus and Cairns, 2014; Granier and Vile, 2014; Fahlgren et al., 2015; Zaman-Allah et
174   al., 2015). Analysis of plant phenotypes, such as size, shape, color, growth, and leaf area
175   altered by herbivory, can be automatically extracted from image data to observe how
176   such traits change over time (Green et al., 2012; Lamari, 2008). Image-based methods are
177   well suited to characterize the spatial and temporal dimensions of disease symptoms and
178   have been applied to several host-pathogen systems (Mahlein et al., 2012; Rousseau et
179   al., 2013; Bauriegel and Herppich, 2014; Baranowski et al., 2015; Li et al., 2015; Raza et
180   al., 2015). These studies illustrate the range of imaging data that can be generated to
181   automate and quantify detection of disease symptoms. Additionally, these studies
182   emphasize that each imaging assay must be calibrated to detect the critical aspects of the
183   pathosystem being studied.

184   Cassava (*Manihot esculenta*) is a major staple crop for an estimated 800 million
185   people in Africa, South America, and Asia (FAO, 2013) and is prized as a drought-
186   tolerant plant that is able to thrive on marginal lands. Among the diseases that impact this

187   crop is cassava bacterial blight (CBB), which is caused by the Gram-negative bacterial

188   pathogen *Xanthomonas axonopodis* pv. *manihotis* (*Xam*). CBB disease symptoms are

189   characterized at early stages by water-soaked lesions on leaves and at later stages of

190   infection by wilting and defoliation (Lozano, 1986). Currently, no disease resistance

191   genes have been demonstrated to be effective against CBB, and chemical methods are not

192   an economically feasible form of control for smallholder farmers. Consequently, novel,

193   genetically encoded methods of achieving plant immunity to CBB must be developed.

194   T3Es that are both conserved in *Xam* populations and important for virulence represent

195   possible targets for engineering durable resistance. Previously, the T3E repertoires for 65

196   *Xam* strains were predicted based on their genomic sequences (Bart et al., 2012). This

197   study predicted 13 to 23 effectors in each strain based on homology to proteins from

198   other systems, excluding the transcriptional activator-like (TAL) effectors that are not

199   resolved by Illumina short read technology. Currently, only a few TAL effectors have

200   been functionally characterized in *Xam* (Castiblanco et al., 2013; Cohn et al., 2014).

201   Notably, several recent studies have explored the use of alternate assays to elucidate the

202   role of T3Es in pathogen virulence (Castiblanco et al., 2013; Cernadas et al., 2014; Cohn

203   et al., 2014).

204   For this study, we focused on homologs of two previously characterized T3Es,

205   AvrBs2 and XopX, and one predicted T3E, XopK, whose role in virulence is unclear.

206   AvrBs2 contains a glycerol phosphodiesterase domain that is required for its virulence

207   functions in other *Xanthomonas* pathovars (Kearney and Staskawicz, 1990; Tai et al.,

208   1999; Zhao et al., 2011; Li et al., 2015). XopX is involved in suppressing pathogen-

209   triggered immunity (Metz et al., 2005; Sinha et al., 2013; Stork et al., 2015). XopK was

210   first identified in the rice pathogen *Xanthomonas oryzae* pv. *oryzae* (*Xoo*) (Furutani et al.,

211   2006). Previous data indicated that XopK is secreted through the type III secretion system

212   (T3SS) into host cells (Furutani et al., 2009; Schulze et al., 2012). Although the *xopK*

213   gene is conserved in many *Xanthomonas* species, its role in virulence is unknown

214   (Bogdanove et al., 2011; Potnis et al., 2011; Bart et al., 2012; Schulze et al., 2012;

215   Arrieta-Ortiz et al., 2013; Jalan et al., 2013).

216   Our efforts to phenotypically characterize these *Xam* mutants began with standard

217   methods such as visual monitoring of symptom development and quantifying bacterial

218   growth *in planta* over the course of several days. These methods were limited in

219   resolution, consistency between experiments, and robustness. Consequently, we sought to

220   apply image-based phenotyping methods to study this pathosystem. The first method

221   addresses issues of human bias during scoring by using a low-cost, Raspberry Pi

222   computer and camera to capture and quantify infection over time. The second approach

223   leverages a bioluminescent reporter system within the bacteria to non-invasively monitor

224   pathogen spread throughout the plant (Meyer et al., 2005; Xu et al., 2010). The

225   combination of these methods achieved unprecedented resolution and sensitivity for

226   quantifying the spatial and temporal dynamics of disease progression within the

227   laboratory setting. The results of this study highlight the importance of adopting a holistic

228   approach to phenotyping plant-pathogen interactions to reveal biological functions of

229   virulence proteins and inform development of disease control strategies.

230

231   **Results**

232   *Pathogen growth levels and symptom development for* Xam *type III effector mutants*

233   To investigate the virulence functions of predicted *Xam* T3Es, we generated

234   mutations in genes homologous to *avrBs2*, *xopX*, and *xopK*. Full gene deletions were

235   created by homologous recombination and initial analysis of pathogen growth levels and

236   symptom development were performed using standard methods (see Materials and

237   Methods) (Whalen et al., 1991; Liu et al., 2015). When inoculated by syringe infiltration

238   in a cassava leaf, wild-type *Xam* populations increased to high levels and caused dark

239   water-soaking symptoms that developed within days of inoculation (Fig. 1). In contrast,

240   mutation of the *hrpF* gene, which encodes a translocon protein required for type III

241   secretion (Buttner et al., 2002), caused a 2-log reduction in pathogen growth levels (Fig.

242   1, A-B) relative to the wild-type strain and eliminated water-soaking disease symptoms

243   (Fig. 1C). For the Δ*avrBs2* and Δ*xopX* mutants, we observed slightly decreased growth

244   levels compared with wild-type over a total of four independent experiments (Fig. 1A,

245   Supplemental Fig. S1). A generalized linear mixed model (GLMM) adjusted by

246   experiment and technical replicates indicated significant differences in pathogen growth

247   at 5 days post inoculation (dpi) for the Δ*hrpF* ($p < 0.001$, $\alpha = 0.05$), Δ*avrBs2* ($p < 0.001$,

248    $\alpha = 0.05$), and Δ*xopX* mutants ($p = 0.0155$, $\alpha = 0.05$), relative to wild-type. At 6 dpi, the

249 Δ*avrBs2* mutant exhibited a reduction in disease symptoms (Fig. 1C). There were no

250 obvious differences, however, in disease symptom production between the Δ*xopX* mutant

251 and wild-type at 6 dpi (Fig. 1C).

252 In contrast to the Δ*avrBs2* and Δ*xopX* mutants, we observed that the Δ*xopK*

253 mutant exhibited pathogen growth levels that were either similar to or elevated compared

254 to wild-type across four experiments (Fig. 1B, Supplemental Fig. S1). A GLMM

255 indicated the growth differences observed for the Δ*xopK* mutant at 5 dpi were not

256 significantly different from wild-type ($p = 0.655$, $\alpha = 0.05$). However, water-soaking

257 disease symptoms caused by the Δ*xopK* mutant appeared enhanced at 6 dpi (Fig. 1C). To

258 address the limitations of visual assessment of disease and to better understand the

259 temporal dimension of this phenotype, we sought to develop a quantitative method of

260 assessing symptom development with increased time resolution.

261

262 *Image-based quantification of disease symptom development*

263 To develop a low-cost imaging system for semi-automated quantification of

264 disease symptom development, we used Raspberry Pi microcomputers and camera boards

265 to image the abaxial side of the leaf during symptom development (Fig. 2A). Following

266 data collection, regions of interest (ROI) were selected manually from the image stacks

267 that contained each inoculated spot, and image analysis was performed using an ImageJ

268 macro script (Fig. 2A, Supplemental Fig. S2).

269 We quantified water-soaking disease symptoms caused by wild-type *Xam*, along

270 with the Δ*xopK* and the Δ*hrpF* mutants (Fig. 2B). For the wild-type strain, disease

271 symptoms began appearing at approximately 100 hours post inoculation. As expected, the

272 Δ*hrpF* mutant did not produce disease symptoms throughout the course of the

273 experiment. For the Δ*xopK* mutant, an increased rate of symptom accumulation was

274 observed relative to the wild-type strain in the initial phase of disease appearance over

275 four separate experiments (Fig. 2B, Supplemental Fig. S3). To compare the rates of

276 symptom accumulation for these strains, we performed a GLMM analysis, adjusted by

277 experiment and technical replicates. Additionally, we adjusted for heteroskedasticity by

278 allowing the variance to be exponentially related to time. This analysis indicated that

279 slopes for both the Δ*hrpF* ($p < 0.0001$, $\alpha = 0.05$) and Δ*xopK* ($p = 0.0476$, $\alpha = 0.05$)

280   mutants were significantly different from wild-type. Thus, despite being a predicted T3E,

281   mutation of the *xopK* gene induces disease symptoms more rapidly during infection than

282   wild-type *Xam*.

283   To further investigate the impacts of other T3E mutations on disease symptom

284   progression, we performed imaging of cassava leaves inoculated with the *Xam* Δ*avrBs2*

285   and Δ*xopX* mutants (Fig. 2C, D). As with the experiments involving the Δ*xopK* mutant,

286   we used GLMM, adjusted by experiment, technical replicates, and heteroskedasticity.

287   The Δ*avrBs2* mutant exhibited significantly decreased disease symptom progression

288   relative to wild-type ($p < 0.0001$, $\alpha = 0.05$), consistent with visual observations of disease

289   (Fig 1). For the Δ*xopX* mutant, while symptom progression appeared slightly delayed

290   compared to wild-type, this effect was not significantly different from wild-type across

291   all experiments ($p = 0.1447$, $\alpha = 0.05$). Thus, in the T3E repertoire of *Xam*, AvrBs2 has a

292   greater contribution to early symptom progression than XopX.

293

294   *Characterizing bacterial spread in host tissue*

295   To observe the ability of T3E mutants to spread systemically during infection, we

296   developed a method to track bacterial spread *in planta*. This is particularly important for

297   *Xam* because it spreads through the host vascular system to cause disease (Lozano, 1986).

298   Therefore, bacterial growth and symptom development at the site of inoculation are

299   descriptive of only a small part of pathogenesis. It has been shown that bioluminescent

300   bacterial strains can be used to detect pathogen presence in host tissue (Bogs et al., 1998;

301   Meyer et al., 2005; Xu et al., 2010).

302   To determine if we could detect *Xam* and visualize spread from an initial infection

303   site *in planta*, we generated bioluminescent strains by introducing a plasmid driving

304   constitutive expression of the LUX operon into *Xam* and the T3E mutants by conjugation.

305   The inoculated areas were imaged in a dark chamber to detect the bioluminescence signal

306   after syringe inoculation of LUX strains into cassava leaves. Local areas infiltrated with

307   wild-type *Xam* exhibited a circular region of bioluminescence that appeared by 4 dpi,

308   followed by spread into surrounding tissues (Fig. 3). This spread extended beyond the

309   visible area of water-soaking symptoms observed at 9 dpi. These results indicate *Xam*

310   proliferates locally at the site of inoculation before invading into the nearby vasculature,

10

311   and that bacterial spread can be observed in regions of the plant that do not yet exhibit

312   visible symptoms.

313   To quantify the changes in bacterial luminescence observed from these images,

314   we applied image analysis methods for measuring both the convex hull area and

315   maximum span across the convex hull, which estimate the total area invaded and the

316   maximum linear distance of spread by the pathogen, respectively. Compared to wild-type

317   *Xam*, the Δ*xopX* mutant exhibited reduced spread, observed in five independent

318   experiments (Fig. 3, Supplemental Fig. S4). A GLMM, adjusted by experiment and

319   technical replicates, indicated at 9 dpi this reduction in spread quantified by convex hull

320   area was statistically significant ($p < 0.0001$, $\alpha = 0.05$). We observed significant

321   reduction in pathogen spread for the Δ*avrBs2* ($p = 0.0388$, $\alpha = 0.05$) and Δ*xopK* mutants

322   ($p = 0.0257$, $\alpha = 0.05$). Further consideration of these data revealed that experimental

323   noise reflected the timing of pathogen entry into the plant vasculature (Fig. 3,

324   Supplemental Fig. S4). These results highlight the importance of invasion into host

325   vasculature by *Xam* for virulence and the power of image-based phenotyping assays for

326   visualizing this dynamic process.

327

328   *Characterizing bacterial spread* in vitro

329   Given the phenotype observed for reduced spread in host tissue, next we

330   examined if any of the T3E mutants affected motility *in vitro* (Supplemental Fig. S5).

331   Bacteria were plated at the center of soft agar plates, which allowed them to spread across

332   the surface of the media (Lee et al., 2003; Tian et al., 2015). Using a Raspberry Pi-

333   controlled camera, images of the plates were taken for several days, and the area of

334   bacterial spread was quantified (Supplemental Fig. S5). We observed that the Δ*hrpF,*

335   Δ*avrBs2*, Δ*xopX*, and Δ*xopK* mutants do not have any apparent motility defects on soft

336   agar. These results suggest that observed defects in mutant movement through host

337   vascular tissue are due to factors other than intrinsic bacterial motility.

338

339   *Imaging bacterial colonization in other pathosystems*

340   Since tracking bacterial colonization with a bioluminescent reporter was

341   successful in cassava, we wanted to expand the use of this method to other pathosystems.

11

342   To explore this, we generated bioluminescent *Xanthomonas campestris* pv. *campestris*

343   (*Xcc*) and *Xanthomonas euvesicatoria* (*Xe*) by conjugation. Following syringe inoculation

344   of bioluminescent *Xam* and *Xcc,* bacteria can be visualized near the site of infection and,

345   in the case of *Xam,* at distal sites following spread into the vasculature (Fig. 4). Since *Xe*

346   infection in pepper and tomato results in leaf spot disease, dip inoculations were used for

347   this strain to mimic field infections. Bioluminescent *Xe* could be readily detected in

348   distinct puncta across the leaf following dip inoculation (Fig. 4). These results

349   demonstrate the utility of bioluminescent technologies to track pathogens in diverse crop

350   plants.

351

352   **Discussion**

353   In complex interactions between hosts and pathogens, T3Es are key targets for

354   resistance strategies. The specific virulence functions of T3Es, however, can be difficult

355   to determine, and their characterization remains a primary goal of researchers within the

356   plant-microbe interaction field. Traditionally, relative virulence of pathogen strains is

357   quantified through visual assessment of plant symptoms and destructive harvesting to

358   measure pathogen populations over time. However, these methods alone often do not

359   provide enough information to make conclusions about T3E functions during infection.

360   Furthermore, CBB has a number of challenges for experimental study. For example, *Xam*

361   is able to spread *in planta* through both mesophyll and vascular tissue (Boher and

362   Verdier, 1994). The pattern of colonization for these distinct tissue types likely

363   contributes to observed experimental noise. Furthermore, cassava plants are propagated

364   from vegetative cuttings, so it is difficult to obtain plants that are developmentally

365   synchronized and physiological aspects of cassava plants such as latex content of leaves

366   may vary from one experiment to another. Finally, it is notable that cassava is a field

367   grown crop with a long generation time (12 months) and development of phenotyping

368   methods from which observations will translate to field setting is desirable.

369   To address these limitations, we applied image-based phenotyping methods that

370   enable quantification of spatial and temporal dynamics for plant-pathogen interactions

371   (Figure 5). Measuring symptom area with increased time resolution, enabled by

372   automated imaging, allowed us to observe an enhanced rate of early disease accumulation

12

373   for the Δ*xopK* mutant. This phenotype demonstrates the importance of a pathogen's

374   ability to establish infection for overall virulence. While XopK is a predicted T3E

375   effector that carries the hallmarks of a secreted virulence factor (Furutani et al., 2006;

376   Furutani et al., 2009; Schulze et al., 2012), its roles during infection appear to be

377   complex. The XopK protein sequence contains 54% hydrophobic residues and several

378   predicted transmembrane domains. Thus, it is possible this protein is associated with host

379   cell membranes following secretion. Our observations for XopK are contrasted with the

380   roles of AvrBs2 and XopX, which exhibit reduced virulence phenotypes, consistent with

381   previous studies (Kearney and Staskawicz, 1990; Metz et al., 2005; Zhao et al., 2011;

382   Sinha et al., 2013; Li et al., 2015; Stork et al., 2015). Our results further illustrate that

383   T3E mutants may impact certain aspects of host-pathogen interactions more than others.

384   For example, XopX contributes more to *Xam* proliferation in the host than to disease

385   symptom progression, while AvrBs2 contributes significantly to both aspects of infection.

386   Thus, combining data from several phenotyping approaches is necessary for determining

387   the roles of T3Es in virulence (Table 1).

388   Another challenge of studying plant-pathogen interactions is visualizing and

389   quantifying a pathogen's location and movement in host tissue. As we observed imaging

390   *Xam* strains in cassava, bioluminescence is a powerful tool for studying the spatial and

391   temporal dimensions of pathogen spread in host tissue. Previously, bioluminescent

392   bacterial strains were used to visualize *Xcc* infection in *Arabidopsis thaliana* (Meyer et

393   al., 2005). Also bioluminescent strains of the tomato pathogen *Clavibacter michiganensis*

394   were used to track bacterial movement following grafting and during germination (Xu et

395   al., 2010). Imaging of bioluminescence with increased spatial resolution allows for

396   quantification of patterns of pathogen spread, as we observed for *Xam* infection in

397   cassava leaves. Our studies visualized the process by which *Xam* invades host

398   vasculature. The experimental variation we observed suggests this is a dynamic process

399   impacted by a range of factors, such as proximity to primary and secondary leaf veins,

400   leaf developmental status, and environmental conditions. These variables can be

401   investigated using our imaging approaches. In particular, environmental factors such as

402   humidity and heat are known to be important for CBB severity in the field (Boher and

403   Verdier, 1994). How these conditions promote disease severity is currently unknown but

13

404 may be related to mechanisms of pathogen spread in host tissue. These factors can be
405 readily explored by direct imaging using an environmentally controlled chamber.

406   While image-based phenotyping approaches offer great promise, characterizing
407 plant-pathogen interactions with such methods also has many challenges, in part due to
408 the diverse range of symptoms and multiple scales at which disease occurs. For each
409 pathosystem, one must first identify the relevant aspects of the infection that can be
410 imaged and the relevant metrics that are needed to characterize the system. This initial
411 study relied on visible light imaging. In future studies, other wavelengths of the
412 electromagnetic spectrum that provide additional information for characterizing disease
413 will be considered. Hyperspectral imaging, which collects spectral data for every pixel,
414 has been used to classify and quantify several diseases that infect sugar beet (Mahlein et
415 al., 2012; Leucker et al., 2016). Thermal imaging offers another approach for detecting
416 disease in plant canopies, since many diseases impact transpiration rates and, therefore,
417 plant surface temperature. While environmental variation can introduce challenges into
418 thermal imaging, Raza et al. addressed this issue by using a combination of thermal and
419 visible light imaging, along with depth estimation, to detect diseased tomato plants using
420 a machine learning approach (Raza et al., 2015). In a laboratory context, fine-scale
421 imaging of disease symptoms on a single leaf may be the optimal approach for
422 investigating certain experimental questions, while whole-plant or field-scale imaging
423 would be necessary for detecting disease in an agricultural context. Unmanned aerial
424 vehicles performing multispectral imaging were used at the field scale to examine abiotic
425 stress in maize (Zaman-Allah et al., 2015). Biotic stresses likely could be detected using
426 similar signatures from aerial imaging.

427   This study presents a new approach to investigation of plant-pathogen
428 interactions. Inspired by the advances of image-based phenotyping methods in other areas
429 of plant biology, we have applied similar methods to quantifying spatial and temporal
430 dimensions of disease development. This approach expands the potential range of
431 phenotypes that can be explored, enabling insights that are difficult to obtain by
432 traditional methods. Since many smallholder farmers in the developing world rely on
433 cassava for food security, low-cost monitoring devices that enable rapid detection of
434 disease outbreaks in the field would be beneficial. In an ideal scenario, monitoring

14

435 devices would be deployed to cassava fields in disease-prone regions and transmit data

436 over wireless networks to give farmers early warning of disease outbreaks. Many

437 technical and logistical challenges would need to be overcome to achieve this goal.

438 However, our image-based methods for detecting disease represent a first step in

439 developing capabilities for such a device. Remote detection of disease through imaging

440 or other means is a promising approach for plant pathology research that can be translated

441 from the laboratory to the field. While characterizing each plant-pathogen system has its

442 own unique challenges, image-based phenotyping methods can be adapted for many

443 systems and offer the potential to revolutionize plant disease identification and

444 quantification.

445

446 **Materials and methods**

447 *Bacterial strains and plant varieties*

448 The following strains of *Xanthomonas axonopodis* pv. *manihotis* (*Xam*) were used:

449 *Xam668*, *Xam668 ΔavrBs2*, *Xam668 ΔhrpF*, *Xam668 ΔxopK*, and *Xam668 ΔxopX*. For

450 experiments performed in cassava (*Manihot esculenta*), variety 60444 was used, except

451 in experiments noted were variety TME7 was used. Strains used for other pathosystems

452 include: *Xanthomonas euvesicatoria* (*Xe* 85-10) and *Xanthomonas campestris* pv.

453 *campestris* (*Xcc* 8004). For experiments in pepper, *Capsicum annuum* variety ECW was

454 used. For experiments in tomato, *Solanum lycopersicum* variety M82 was used. For

455 experiments in broccoli, *Brassica oleracea*, was used.

456

457 *Generation of bacterial mutants*

458 To generate gene deletion mutants in bacteria, we used a homologous

459 recombination strategy, in which genomic regions flanking each gene of interest were

460 first cloned into the pENTR-d-TOPO vector (Invitrogen). Blunt-end cloning of the PCR

461 products was performed to introduce the PCR fragments into pENTR-d-TOPO.

462 Restriction sites added with the primers were used to create a version of the vector with 5'

463 and 3' flanking regions adjacent to each other. Gateway cloning was used to transfer this

464 cassette into the pLVC18-sacBR vector, which enabled a sucrose counter-selection

465 approach to be used in creating unmarked gene deletions (Logue et al., 2009). This vector

466   was conjugated into *Xam* using a triparental mating system, with an *E. coli* helper strain

467   containing the pRK600 plasmid. Mutants with the unmarked gene knockout were

468   confirmed with PCR.

469

470   *Bacterial inoculations and growth monitoring* in planta

471   To quantify bacterial growth in plant tissue, leaves were inoculated with solutions

472   of bacterial strains (OD_{600} = 0.0001) re-suspended in 10 mM $MgCl_2$. Prior to inoculation,

473   the leaf was wounded with a razor blade, and the bacterial solutions were injected into the

474   leaf with a needleless 1-mL syringe. Approximately 0.1 mL of bacterial solution was

475   injected at each inoculation site.

476   For each time point that bacterial growth was monitored, leaf punches were taken

477   from inoculated regions. A 1-cm diameter cork borer was used to excise a leaf disk,

478   which was then ground with a tungsten carbide bead in 200 μL of 10 mM $MgCl_2$ using a

479   TissueLyser (Qiagen). Dilutions of the leaf lysate were then plated on NYG agar media

480   with 100 μg $μL^{-1}$ rifampicin, and *Xam* colonies were counted to estimate the number of

481   bacteria in the original leaf sample.

482

483   *Image acquisition and analysis for quantification of disease symptoms*

484   Leaves were inoculated with solutions of bacterial strains (OD_{600} = 0.001). The

485   leaves were then taped to a black surface, such that the abaxial side of the leaf faced

486   downward toward a camera. Images of disease symptoms were taken with Raspberry Pi

487   5MP camera boards controlled by Raspberry Pi Model B microcomputers. Hourly

488   automated image collection was done with Cron. For all experiments shown, images were

489   taken hourly. Image stacks were analyzed with FIJI, running ImageJ version 2.0.0-rc-

490   30/1.49v (Schindelin et al., 2012; Schindelin et al., 2015). The scale of the image stacks

491   was determined with a ruler included in the image, enabling unit conversion from pixels

492   to cm.

493   A region of interest (ROI) was selected that contained each inoculated area. An

494   ImageJ macro script was used to select and quantify the area of water-soaking symptoms

495   for each ROI (Supplemental File S1). The ROI stacks were converted to HSB (hue-

496   saturation-brightness) color space. After selecting the saturation channel, a background

16

497 subtraction was performed. Then, the area of disease was selected by creating a binary

498 image with black pixels representing symptomatic regions and white pixels representing

499 non-symptomatic tissue. The binary images were created by applying a threshold

500 calculated by the following,

$$t = \mu - n\sigma$$

501 where t = threshold, μ = mean saturation value of the ROI stack, and σ = standard

502 deviation of saturation values for the ROI stack. For the variable n, a range of values

503 were tested to determine the appropriate threshold for selecting disease symptoms. The

504 area of black pixels in the binary images was then quantified to determine the area of

505 disease symptoms for each ROI.

506

507 *Bioluminescence imaging and analysis*

508   Bioluminescent bacteria were generated by conjugating the pLUX plasmid into

509 *Xanthomonas* strains of interest. Leaves were inoculated with solutions of these strains

510 (OD_{600} = 0.01), with one strain inoculated per leaf lobe. Images were taken using a Star I

511 CCD digital camera system (Photometrics Ltd.) or a PIXIS 1024B (Princeton

512 Instruments) that was contained in a blackout chamber. The cameras were operated with

513 WinView/32 software version 2.5.22.0 (Princeton Instruments) or μManager v1.4.22

514 (Open Imaging), respectively.

515   Using ImageJ, each image was converted to an 8-bit TIFF file. Then, the Auto

516 Enhance Contrast function was applied, and a binary image was created with the Auto

517 Threshold function using the MaxEntropy algorithm (Kapur et al., 1985). Next, the

518 Despeckle and Invert functions were applied to create an image in which the

519 bioluminescent signal was represented by black pixels. Finally, the Hull and Circle plugin

520 v2.1b (http://rsb.info.nih.gov/ij/plugins/hull-circle.html) was used to select and quantify

521 the convex hull for each shape representing the bioluminescence signal.

522

523 In vitro *bacterial motility assays*

524   The ability of *Xam* strains to spread *in vitro* was observed on NYG media

525 containing 0.25% agar and 100 μg μL^{-1} rifampicin. 10 μL of a bacterial solution (OD_{600} =

526 0.1) was spotted in the center of each plate. A Raspberry Pi camera was set to image the

17

527 plates from a top-view. Images of the plates were taken over several days, as the bacteria

528 spread from the center of the plates. The ROI containing the bacterial colony on each

529 plate was selected, and an ImageJ macro script was used to create a binary image where

530 black pixels represented the area of the bacterial colony (Supplemental File S2). The

531 number of black pixels was then quantified to determine the bacterial area on the plate.

532

533 *Data and statistical analysis*

534   All graphs and data analyses were generated with R version 3.1.3 (R Core Team,

535 2015), using the following packages: ggplot2 version 1.0.1 (Wickham, 2009), knitr

536 version 1.11 (Xie, 2015), lme4 version 1.1-11 (Bates et al., 2015), lsmeans version 2.20-

537 23 (Lenth, 2015), multcomp version 1.4-4 (Hothorn et al., 2008), nlme version 3.1-128

538 (Pinheiro et al. 2016), plyr version 1.8.3 (Wickham, 2011), reshape2 version 1.4.1

539 (Wickham, 2007), and scales version 0.3.0 (Wickham, 2015). For each data set, a

540 generalized linear mixed model was used to assess the responses as a function of different

541 bacterial strains and over time while adjusting for correlation structures due to repeated

542 measures and cross-experimental variation. After the models were fit and checked for

543 underlying assumptions, statistical contrasts were implemented using a post hoc Tukey's

544 t test to compare the effect of interest across the different bacterial strains using an α level

545 of 0.05 as the cutoff for statistical significance.

546

547 **Supplemental material**

548 The following supplemental materials are available.

549

550 Supplemental Figure S1. Replicate experiments for analysis of *Xam* T3E mutant growth

551 *in planta* shown in Fig. 1.

552

553 Supplemental Figure S2. Image analysis optimization for water-soaking disease

554 symptoms caused by *Xam*.

555

556 Supplemental Figure S3. Replicate experiments for analysis of water-soaking symptoms

557 shown in Fig. 2.

558

559   Supplemental Figure S4. Replicate experiments for analysis of *Xam* spread in leaves
560   using bioluminescence imaging shown in Fig. 4.

561

562   Supplemental Figure S5. *In vitro* motility of *Xam* T3E mutants.

563

564   Supplemental File S1. ImageJ macro script used to quantify water-soaking disease
565   symptoms.

566

567   Supplemental File S2. ImageJ macro script used to quantify bacterial spread on soft agar
568   plates.

569

570   **Acknowledgments**
571   We would like to thank Malia Gehan and Noah Fahlgren for their help with the image
572   acquisition and analysis.

573

574   **Figure legends**
575   **Figure 1.** Disease symptom development and growth levels for *Xam* type III effector
576   (T3E) mutants in cassava. A-B, Growth levels of *Xam* wild-type, Δ*hrpF*, Δ*avrBs2*,
577   Δ*xopX*, and Δ*xopK* mutants following syringe infiltration in leaves (OD$_{600}$ = 0.0001).
578   Median, first and third quartiles are shown. The whiskers extend to the highest and lowest
579   data point falling within 1.5*IQR (inter-quartile range). Dots represent outliers that fall
580   outside 1.5*IQR. Each experiment was repeated three additional times (see Supplemental
581   Fig. S1). C, Comparison of disease symptoms caused by T3E mutants on leaves at 6 days
582   after syringe infiltration (OD$_{600}$ = 0.0001). D, Results of generalized linear mixed model
583   analysis, combining bacterial growth data from all replicate experiments. Combined
584   estimated means and standard error (SE) are presented, as well as the difference between
585   the means and the p-values for each pairwise statistical contrast.

586

587   **Figure 2.** Quantification of disease symptoms caused by *Xam* on cassava leaves using
588   imaging. A, Illustration of the imaging set-up. Leaves were syringe infiltrated with

19

589   bacterial solutions ($OD_{600} = 0.001$) and taped to a black surface for imaging of the abaxial

590   side of the leaf. Raspberry Pi microcomputer with attached camera collected images once

591   per hour. Image analysis steps in ImageJ are shown and described in Materials and

592   Methods. The number of black pixels was quantified to determine the area of disease. B-

593   D, Quantification of water-soaking symptoms caused by the *Xam* wild-type strain and

594   three mutants over time. Dots represent individual measurements determined from image

595   analysis, and local regression fitted curves are plotted for each bacterial strain. Shaded

596   areas represent the 95% confidence interval for each curve. The experiment was repeated

597   three additional times with similar results (see Supplemental Fig. S3). E, Results of

598   generalized linear mixed model analysis, combining data from all replicate experiments.

599   Combined estimated slopes and standard error (SE) are presented, as well as p values for

600   each pairwise statistical contrast.

601

602   **Figure 3.** Bioluminescence imaging of *Xam* spread in cassava leaves. A, The

603   bioluminescence reporter pLUX plasmid was introduced into *Xam* strains. Leaves were

604   inoculated with bacterial solutions ($OD_{600} = 0.01$) using syringe infiltration. RGB images

605   of inoculated leaves reveal symptom development. Bioluminescence was visualized in a

606   dark chamber with a 5-10 min exposure. Image processing was performed with ImageJ to

607   select the area of bioluminescence and the convex hull of the resulting shapes were

608   analyzed. B, Representative quantification of convex hull for wildtype Xam and three

609   mutants. Additional replicate experiments are shown in Supplemental Fig. S4. C, Results

610   of generalized linear mixed model analysis of convex hull area, combining data from all

611   replicate experiments. Combined estimated means and standard error (SE) are presented,

612   as well as the difference between the means and the p-values for each pairwise statistical

613   contrast.

614

615   **Figure 4.** Comparison of vascular and leaf spot pathogens. *Xam* and *Xcc* were visualized

616   following syringe inoculation ($OD_{600} = 0.01$) at 18 days post inoculation (dpi) and 12 dpi,

617   respectively. Bacterial spot on pepper and tomato were visualized following dip

618   inoculation ($OD_{600} = 0.5$) of *Xe* at 9 dpi.

619

20

620   **Figure 5.** Summary for type III effector mutant phenotypes as revealed by different
621   phenotyping methods.

622

623   **Supplemental Figure S1.** Replicate experiments for analysis of *Xam* T3E mutant growth
624   *in planta* shown in Figure 1. A-C, Three additional experiments to quantify growth levels
625   of the *Xam* wild type strain, and the *Xam* Δ*hrpF*, Δ*avrBs2*, and Δ*xopX* mutants following
626   syringe infiltration in leaves (OD_{600} = 0.0001). D-F, Three additional experiments to
627   quantify growth levels of wild-type *Xam*, and the Δ*hrpF* and Δ*xopK* mutants following
628   syringe infiltration in leaves (OD_{600} = 0.0001).

629

630   **Supplemental Figure S2.** Image analysis optimization for water-soaking disease
631   symptoms caused by *Xam*. Following conversion of regions of interest (ROI) to hue-
632   saturation-brightness (HSB) color space and background subtraction, the distributions of
633   pixel values for each channel were examined. Disease symptoms are best represented by
634   pixel values in the lower tail of the distribution for the saturation channel. A range of
635   threshold values were applied to the images to create binary images, according to the
636   formula $t = \mu - n\sigma$, where t = threshold, μ = mean saturation value for the image stack,
637   and σ = standard deviation of saturation values for the image stack. Graphs show
638   example thresholds where n = 3 (blue line), n = 2.5 (red line), and n = 2 (green line). The
639   binary images on the right show the results of applying the n = 3 threshold.

640

641   **Supplemental Figure S3.** Three additional replicate experiments for analysis of water-
642   soaking symptoms shown in Fig. 2. Dots represent individual measurements determined
643   from image analysis, and local regression fitted curves are plotted for each bacterial
644   strain. Shaded areas represent the 95% confidence interval for each curve. For the
645   experiment shown in A, the image distances were not scaled to cm, so values are reported
646   in pixels. Experiments shown in panels D-F and H-I were performed with cassava variety
647   TME7.

648

649   **Supplemental Figure S4.** Replicate experiments for analysis of *Xam* spread in leaves
650   using bioluminescence imaging shown in Fig. 3. Three additional experiments

21

651 quantifying the convex hull area for the *Xam* Δ*xopX* (A-C)*, ΔavrBs2* (D-F), and Δ*xopK*

652 (G-I) mutants. Quantification of the maximum span across the convex hull for the same

653 experiments (K-S). Quantification of the convex hull area (T) and maximum span (U) for

654 a fourth replicate experiment including the three mutants. Dots represent individual

655 measurements; lines connect the mean at each time point. V, Results of generalized linear

656 mixed model analysis for maximum span results, combining data from all replicate

657 experiments. Combined estimated means and standard error (SE) are presented, as well as

658 p values for each pairwise statistical contrast.

659

660 **Supplemental Figure S5.** *In vitro* motility of *Xam* T3E mutants. Bacteria were spotted in

661 the center of plates containing NYG media with 0.25% agar. Images were taken of the

662 plates over several days, and the area of bacterial spread was quantified using ImageJ. A,

663 Example of binary thresholding used to select the area of bacterial spread from the

664 images. B-D, Quantification of bacterial spread for the *Xam* T3E mutants, relative to the

665 wild-type strain. Dots represent individual data points, and local regression fitted curves

666 are plotted for each bacterial strain. Shaded areas represent the 95% confidence interval

667 for each strain.

668

669 REFERENCES
670
671 Araus JL, Cairns JE (2014) Field high-throughput phenotyping: the new crop breeding
672   frontier. Trends Plant Sci 19: 52-61
673 Arrieta-Ortiz ML, Rodriguez RL, Perez-Quintero AL, Poulin L, Diaz AC, Arias Rojas N,
674   Trujillo C, Restrepo Benavides M, Bart R, Boch J, Boureau T, Darrasse A, David
675   P, Duge de Bernonville T, Fontanilla P, Gagnevin L, Guerin F, Jacques MA,
676   Lauber E, Lefeuvre P, Medina C, Medina E, Montenegro N, Munoz Bodnar A,
677   Noel LD, Ortiz Quinones JF, Osorio D, Pardo C, Patil PB, Poussier S, Pruvost O,
678   Robene-Soustrade I, Ryan RP, Tabima J, Urrego Morales OG, Verniere C,
679   Carrere S, Verdier V, Szurek B, Restrepo S, Lopez C, Koebnik R, Bernal A
680   (2013) Genomic survey of pathogenicity determinants and VNTR markers in the
681   cassava bacterial pathogen *Xanthomonas axonopodis* pv. *Manihotis* strain
682   CIO151. PLOS One 8: e79704
683 Baltrus DA, Nishimura MT, Romanchuk A, Chang JH, Mukhtar MS, Cherkis K, Roach J,
684   Grant SR, Jones CD, Dangl JL (2011) Dynamic evolution of pathogenicity
685   revealed by sequencing and comparative genomics of 19 *Pseudomonas syringae*
686   isolates. PLOS Pathog 7: e1002132

22

687 Baranowski P, Jedryczka M, Mazurek W, Babula-Skowronska D, Siedliska A,
688   Kaczmarek J (2015) Hyperspectral and thermal imaging of oilseed rape (*Brassica*
689   *napus*) response to fungal species of the genus *Alternaria*. PLOS One 10:
690   e0122913
691 Bart R, Cohn M, Kassen A, McCallum EJ, Shybut M, Petriello A, Krasileva K, Dahlbeck
692   D, Medina C, Alicai T, Kumar L, Moreira LM, Neto JR, Verdier V, Santana MA,
693   Kositcharoenkul N, Vanderschuren H, Gruissem W, Bernal A, Staskawicz BJ
694   (2012) High-throughput genomic sequencing of cassava bacterial blight strains
695   identifies conserved effectors to target for durable resistance. Proc Natl Acad Sci
696   USA 109: 13130-13130
697 Bates D, Maechler M, Bolker B, Walker S (2015) Fitting linear mixed-effects models
698   using lme4. J Stat Softw 67: 1-48
699 Bauriegel E, Herppich W (2014) Hyperspectral and chlorophyll fluorescence imaging for
700   early detection of plant diseases, with special reference to *Fusarium* spec.
701   infections on wheat. Agriculture 4: 32-57
702 Boch J, Bonas U, Lahaye T (2014) TAL effectors - pathogen strategies and plant
703   resistance engineering. New Phytol 204: 823-832
704 Bock CH, Poole GH, Parker PE, Gottwald TR (2010) Plant disease severity estimated
705   visually, by digital photography and image analysis, and by hyperspectral
706   imaging. Crit Rev Plant Sci 29: 59-107
707 Bogdanove AJ, Koebnik R, Lu H, Furutani A, Angiuoli SV, Patil PB, Van Sluys MA,
708   Ryan RP, Meyer DF, Han SW, Aparna G, Rajaram M, Delcher AL, Phillippy
709   AM, Puiu D, Schatz MC, Shumway M, Sommer DD, Trapnell C, Benahmed F,
710   Dimitrov G, Madupu R, Radune D, Sullivan S, Jha G, Ishihara H, Lee SW,
711   Pandey A, Sharma V, Sriariyanun M, Szurek B, Vera-Cruz CM, Dorman KS,
712   Ronald PC, Verdier V, Dow JM, Sonti RV, Tsuge S, Brendel VP, Rabinowicz
713   PD, Leach JE, White FF, Salzberg SL (2011) Two new complete genome
714   sequences offer insight into host and tissue specificity of plant pathogenic
715   *Xanthomonas* spp. J Bacteriol 193: 5450-5464
716 Bogs J, Bruchmüller I, Erbar C, Geider K (1998) Colonization of host plants by the fire
717   blight pathogen *Erwinia amylovora* marked with genes for bioluminescence and
718   fluorescence. Phytopathology 88: 416-421
719 Boher B, Verdier V (1994) Cassava bacterial blight in Africa: the state of knowledge and
720   implications for designing control strategies. Afr Crop Sci J 2: 505-509
721 Buttner D, Nennstiel D, Klusener B, Bonas U (2002) Functional analysis of HrpF, a
722   putative type III translocon protein from *Xanthomonas campestris* pv. *vesicatoria*.
723   J Bacteriol 184: 2389-2398
724 Castañeda A, Reddy JD, El-Yacoubi B, Gabriel DW (2005) Mutagenesis of all eight *avr*
725   genes in *Xanthomonas campestris* pv. *campestris* had no detected effect on
726   pathogenicity, but one *avr* gene affected race specificity. Mol Plant Microbe
727   Interact 18: 1306-1317
728 Castiblanco LF, Gil J, Rojas A, Osorio D, Gutierrez S, Munoz-Bodnar A, Perez-Quintero
729   AL, Koebnik R, Szurek B, Lopez C, Restrepo S, Verdier V, Bernal AJ (2013)
730   TALE1 from *Xanthomonas axonopodis* pv. *manihotis* acts as a transcriptional
731   activator in plant cells and is important for pathogenicity in cassava plants. Mol
732   Plant Pathol 14: 84-95

733 Cernadas RA, Doyle EL, Nino-Liu DO, Wilkins KE, Bancroft T, Wang L, Schmidt CL,
734   Caldo R, Yang B, White FF, Nettleton D, Wise RP, Bogdanove AJ (2014) Code-
735   assisted discovery of TAL effector targets in bacterial leaf streak of rice reveals
736   contrast with bacterial blight and a novel susceptibility gene. PLOS Pathog 10:
737   e1003972
738 Chakraborty S, Newton AC (2011) Climate change, plant diseases and food security: an
739   overview. Plant Pathol 60: 2-14
740 Cohn M, Bart RS, Shybut M, Dahlbeck D, Gomez M, Morbitzer R, Hou BH, Frommer
741   WB, Lahaye T, Staskawicz BJ (2014) *Xanthomonas axonopodis* virulence is
742   promoted by a transcription activator-like effector-mediated induction of a
743   SWEET sugar transporter in cassava. Mol Plant Microbe Interact 27: 1186-1198
744 Cunnac S, Chakravarthy S, Kvitko BH, Russell AB, Martin GB, Collmer A (2011)
745   Genetic disassembly and combinatorial reassembly identify a minimal functional
746   repertoire of type III effectors in *Pseudomonas syringae*. Proc Natl Acad Sci USA
747   108: 2975-2980
748 Dunger G, Garofalo CG, Gottig N, Garavaglia BS, Rosa MC, Farah CS, Orellano EG,
749   Ottado J (2012) Analysis of three *Xanthomonas axonopodis* pv. *citri* effector
750   proteins in pathogenicity and their interactions with host plant proteins. Mol Plant
751   Pathol 13: 865-876
752 Fahlgren N, Gehan MA, Baxter I (2015) Lights, camera, action: high-throughput plant
753   phenotyping is ready for a close-up. Curr Opin Plant Biol 24C: 93-99
754 FAO (2013) Save and grow: cassava. A guide to sustainable production intensification.
755 Fiorani F, Schurr U (2013) Future scenarios for plant phenotyping. Annu Rev Plant Biol
756   64: 267-291
757 Furbank RT, Tester M (2011) Phenomics--technologies to relieve the phenotyping
758   bottleneck. Trends Plant Sci 16: 635-644
759 Furutani A, Nakayama T, Ochiai H, Kaku H, Kubo Y, Tsuge S (2006) Identification of
760   novel HrpXo regulons preceded by two cis-acting elements, a plant-inducible
761   promoter box and a -10 box-like sequence, from the genome database of
762   *Xanthomonas oryzae* pv. *oryzae*. FEMS Microbiol Lett 259: 133-141
763 Furutani A, Takaoka M, Sanada H, Noguchi Y, Oku T, Tsuno K, Ochiai H, Tsuge S
764   (2009) Identification of novel type III secretion effectors in *Xanthomonas oryzae*
765   pv. *oryzae*. Mol Plant Microbe Interact 22: 96-106
766 Granier C, Vile D (2014) Phenotyping and beyond: modelling the relationships between
767   traits. Curr Opin Plant Biol 18C: 96-102
768 Green JM, Appel H, Rehrig EM, Harnsomburana J, Chung J-F, Balint-Kurti P, Shyu C-R
769   (2012) PhenoPhyte: a flexible affordable method to quantify 2D phenotypes from
770   imagery. Plant Methods 8: 45
771 Hothorn T, Bretz F, Westfall P (2008) Simultaneous inference in general parametric
772   models. Biometrical J 50: 346-363
773 Jalan N, Kumar D, Andrade MO, Yu F, Jones JB, Graham JH, White FF, Setubal JC,
774   Wang N (2013) Comparative genomic and transcriptome analyses of pathotypes
775   of *Xanthomonas citri* subsp. *citri* provide insights into mechanisms of bacterial
776   virulence and host range. BMC Genomics 14: 551

Kapur IN, Sahoo PK, Wong AKC (1985) A new method for the gray-level picture thresholding using the entropy of the histogram. Comput Vision Graph 29: 273-285

Kearney B, Staskawicz BJ (1990) Widespread distribution and fitness contribution of Xanthomonas campestris avirulence gene *avrBs2*. Nature 386: 385-386

Khan M, Subramaniam R, Desveaux D (2016) Of guards, decoys, baits and traps: pathogen perception in plants by type III effector sensors. Curr Opin Microbiol 29: 49-55

Kvitko BH, Park DH, Velasquez AC, Wei CF, Russell AB, Martin GB, Schneider DJ, Collmer A (2009) Deletions in the repertoire of *Pseudomonas syringae* pv. *tomato* DC3000 type III secretion effector genes reveal functional overlap among effectors. PLOS Pathog 5: e1000388

Lacombe S, Rougon-Cardoso A, Sherwood E, Peeters N, Dahlbeck D, van Esse HP, Smoker M, Rallapalli G, Thomma BP, Staskawicz B, Jones JD, Zipfel C (2010) Interfamily transfer of a plant pattern-recognition receptor confers broad-spectrum bacterial resistance. Nat Biotechnol 28: 365-369

Lamari L (2008) Assess 2.0: image analysis software for plant disease quantification. American Phytopathological Society, St. Paul, MN.

Lee M-C, Weng S-F, Tseng Y-H (2003) Flagellin gene *fliC* of *Xanthomonas campestris* is upregulated by transcription factor Clp. Biochem Biophys Res Comm 307: 647-652

Lenth R (2015) lsmeans: least-squares means. R package version 2.20-23. http://CRAN.R-project.org/package=lsmeans

Leucker M, Mahlein AK, Steiner U, Oerke EC (2016) Improvement of lesion phenotyping in *Cercospora beticola*-sugar beet interaction by hyperspectral imaging. Phytopathology 106: 177-184

Li B, Hulin MT, Brain P, Mansfield JW, Jackson RW, Harrison RJ (2015) Rapid, automated detection of stem canker symptoms in woody perennials using artificial neural network analysis. Plant Methods 11: 57

Li S, Wang Y, Wang S, Fang A, Wang J, Liu L, Zhang K, Mao Y, Sun W (2015) The type III effector AvrBs2 in *Xanthomonas oryzae* pv. *oryzicola* suppresses rice immunity and promotes disease development. Mol Plant Microbe Interact 28: 869-880

Li T, Liu B, Spalding MH, Weeks DP, Yang B (2012) High-efficiency TALEN-based gene editing produces disease-resistant rice. Nat Biotechnol 30: 390-392

Lindeberg M, Cunnac S, Collmer A (2012) *Pseudomonas syringae* type III effector repertoires: last words in endless arguments. Trends Microbiol 20: 199-208

Liu X, Sun Y, Korner CJ, Du X, Vollmer ME, Pajerowska-Mukhtar KM (2015) Bacterial leaf infiltration assay for fine characterization of plant defense responses using the *Arabidopsis thaliana-Pseudomonas syringae* pathosystem. J Vis Exp 104: e53364

Logue CA, Peak IR, Beacham IR (2009) Facile construction of unmarked deletion mutants in *Burkholderia pseudomallei* using *sacB* counter-selection in sucrose-resistant and sucrose-sensitive isolates. J Microbiol Methods 76: 320-323

Lozano JC (1986) Cassava bacterial blight: a manageable disease. Plant Disease 70: 1089-1093

822　Macho AP, Zipfel C (2014) Plant PRRs and the activation of innate immune signaling.
823　　　　Mol Cell 54: 263-272
824　Mahlein AK, Steiner U, Hillnhütter C, Dehne HW, Oerke EC (2012) Hyperspectral
825　　　　imaging for small-scale analysis of symptoms caused by different sugar beet
826　　　　diseases. Plant Methods 8: 3
827　Metz M, Dahlbeck D, Morales CQ, Al Sady B, Clark ET, Staskawicz BJ (2005) The
828　　　　conserved *Xanthomonas campestris* pv. *vesicatoria* effector protein XopX is a
829　　　　virulence factor and suppresses host defense in *Nicotiana benthamiana*. Plant J
830　　　　41: 801-814
831　Meyer D, Lauber E, Roby D, Arlat M, Kroj T (2005) Optimization of pathogenicity
832　　　　assays to study the *Arabidopsis thaliana-Xanthomonas campestris* pv. *campestris*
833　　　　pathosystem. Mol Plant Pathol 6: 327-333
834　Pinheiro J, Bates D, DebRoy S, Sarkar D, R Core Team (2016) nlme: linear and
835　　　　nonlinear mixed effects models. R package version 3.1-128. http://CRAN.R-
836　　　　project.org/package=nlme
837　Poland JA, Nelson RJ (2011) In the eye of the beholder: the effect of rater variability and
838　　　　different rating scales on QTL mapping. Phytopathology 101: 290-298
839　Potnis N, Krasileva K, Chow V, Almeida NF, Patil PB, Ryan RP, Sharlach M, Behlau F,
840　　　　Dow JM, Momol MT, White FF, Preston JF, Vinatzer BA, Koebnik R, Setubal
841　　　　JC, Norman DJ, Staskawicz BJ, Jones JB (2011) Comparative genomics reveals
842　　　　diversity among xanthomonads infecting tomato and pepper. BMC Genomics 12:
843　　　　146
844　R Core Team (2015) R: A language and environment for statistical computing. R
845　　　　Foundation for Statistical Computing, Vienna, Austria URL http://www.R-
846　　　　project.org/
847　Raza SE, Prince G, Clarkson JP, Rajpoot NM (2015) Automatic detection of diseased
848　　　　tomato plants using thermal and stereo visible light images. PLOS One 10:
849　　　　e0123262
850　Rousseau C, Belin E, Bove E, Rousseau D, Fabre F, Berruyer R, Guillaumès J, Manceau
851　　　　C, Jacques MA, Boureau T (2013) High throughput quantitative phenotyping of
852　　　　plant resistance using chlorophyll fluorescence image analysis. Plant Methods 9:
853　　　　17
854　Roux B, Bolot S, Guy E, Denance N, Lautier M, Jardinaud MF, Fischer-Le Saux M,
855　　　　Portier P, Jacques MA, Gagnevin L, Pruvost O, Lauber E, Arlat M, Carrere S,
856　　　　Koebnik R, Noel LD (2015) Genomics and transcriptomics of *Xanthomonas*
857　　　　*campestris* species challenge the concept of core type III effectome. BMC
858　　　　Genomics 16: 975
859　Schindelin J, Arganda-Carreras I, Frise E, Kaynig V, Longair M, Pietzsch T, Preibisch S,
860　　　　Rueden C, Saalfeld S, Schmid B, Tinevez JY, White DJ, Hartenstein V, Eliceiri
861　　　　K, Tomancak P, Cardona A (2012) Fiji: an open-source platform for biological-
862　　　　image analysis. Nat Methods 9: 676-682
863　Schindelin J, Rueden CT, Hiner MC, Eliceiri KW (2015) The ImageJ ecosystem: An
864　　　　open platform for biomedical image analysis. Mol Reprod Dev 82: 518-529
865　Schoonbeek HJ, Wang HH, Stefanato FL, Craze M, Bowden S, Wallington E, Zipfel C,
866　　　　Ridout CJ (2015) Arabidopsis EF-Tu receptor enhances bacterial disease
867　　　　resistance in transgenic wheat. New Phytol 206: 606-613

868   Schornack S, Moscou MJ, Ward ER, Horvath DM (2013) Engineering plant disease
869   resistance based on TAL effectors. Annu Rev Phytopathol 51: 383-406
870   Schulze S, Kay S, Buttner D, Egler M, Eschen-Lippold L, Hause G, Kruger A, Lee J,
871   Muller O, Scheel D, Szczesny R, Thieme F, Bonas U (2012) Analysis of new type
872   III effectors from *Xanthomonas* uncovers XopB and XopS as suppressors of plant
873   immunity. New Phytol 195: 894-911
874   Sinha D, Gupta MK, Patel HK, Ranjan A, Sonti RV (2013) Cell wall degrading enzyme
875   induced rice innate immune responses are suppressed by the type 3 secretion
876   system effectors XopN, XopQ, XopX and XopZ of *Xanthomonas oryzae* pv.
877   *oryzae*. PLOS One 8: e75867
878   Stam R, Mantelin S, McLellan H, Thilliez G (2014) The role of effectors in nonhost
879   resistance to filamentous plant pathogens. Front Plant Sci 5: 582
880   Stork W, Kim JG, Mudgett MB (2015) Functional analysis of plant defense suppression
881   and activation by the *Xanthomonas* core type III effector XopX. Mol Plant
882   Microbe Interact 28: 180-194
883   Strauß T, van Poecke RMP, Strauß A, Römer P, Minsavage GV, SIngh S, Wolf C, Strauß
884   A, Kim S, Lee H-A, Yeom SI, Parniske M, Stall RE, Jones JB, Choi D, Prins M,
885   Lahaye T (2012) RNA-seq pinpoints a *Xanthomonas* TAL-effector activated
886   resistance gene in a large-crop genome. Proc Natl Acad Sci USA 109: 19480-
887   19485
888   Tai T, Dahlbeck D, Clark ET, Gajiwala P, Paison R, Whalen MC, Stall RE, Staskawicz
889   BJ (1999) Expression of the *Bs2* pepper gene confers resistance to bacterial spot
890   disease in tomato. Proc Natl Acad Sci USA 96: 14153-14158
891   Teper D, Burstein D, Salomon D, Gershovitz M, Pupko T, Sessa G (2016) Identification
892   of novel *Xanthomonas euvesicatoria* type III effector proteins by a machine-
893   learning approach. Mol Plant Pathol 17: 398-411
894   Tian F, Yu C, Li H, Wu X, Li B, Chen H, Wu M, He C (2015) Alternative sigma factor
895   RpoN2 is required for flagellar motility and full virulence of *Xanthomonas oryzae*
896   pv. *oryzae*. Microbiol Res 170: 177-183
897   Tornero P, Dangl JL (2001) A high-throughput method for quantifying growth of
898   phytopathogenic bacteria in *Arabidopsis thaliana*. Plant J 28: 475-481
899   Tripathi JN, Lorenzen J, Bahar O, Ronald P, Tripathi L (2014) Transgenic expression of
900   the rice *Xa21* pattern-recognition receptor in banana (*Musa* sp.) confers resistance
901   to *Xanthomonas campestris* pv. *musacearum*. Plant Biotechnol J 12: 663-673
902   Wei HL, Chakravarthy S, Mathieu J, Helmann TC, Stodghill P, Swingle B, Martin GB,
903   Collmer A (2015) *Pseudomonas syringae* pv. *tomato* DC3000 type III secretion
904   effector polymutants reveal an interplay between HopAD1 and AvrPtoB. Cell
905   Host Microbe 17: 752-762
906   Whalen MC, Innes RW, Bent AF, Staskawicz BJ (1991) Identification of *Pseudomonas
907   syringae* pathogens of *Arabidopsis* and a bacterial locus determining avirulence
908   on both *Arabidopsis* and soybean. Plant Cell 3: 49-59
909   White FF, Potnis N, Jones JB, Koebnik R (2009) The type III effectors of *Xanthomonas*.
910   Mol Plant Pathol 10: 749-766
911   Wickham H (2007) Reshaping Data with the reshape package. Journal of Stat Softw 21:
912   1-20. URL http://www.jstatsoft.org/v21/i12/
913   Wickham H (2009) ggplot2: elegant graphics for data analysis, Springer New York

914 Wickham H (2011) The split-apply-combine strategy for data analysis. Journal of Stat
915   Softw 40: 1-29. URL http://www.jstatsoft.org/v40/i01/
916 Wickham H (2015) scales: scale functions for visualization. R package version 0.3.0.
917   http://CRAN.R-project.org/package=scales.
918 Win J, Chaparro-Garcia A, Belhaj K, Saunders DG, Yoshida K, Dong S, Schornack S,
919   Zipfel C, Robatzek S, Hogenhout SA, Kamoun S (2012) Effector biology of
920   plant-associated organisms: concepts and perspectives. Cold Spring Harb Symp
921   Quant Biol 77: 235-247
922 Xie W, Yu K, Pauls KP, Navabi A (2012) Application of image analysis in studies of
923   quantitative disease resistance, exemplified using common bacterial blight-
924   common bean pathosystem. Phytopathology 102: 434-442
925 Xie Y (2015) knitr: a general-purpose package for dynamic report generation in R. R
926   package version 1.11.
927 Xu X, Miller SA, Baysal-Gurel F, Gartemann KH, Eichenlaub R, Rajashekara G (2010)
928   Bioluminescence imaging of *Clavibacter michiganensis* subsp. *michiganensis*
929   infection of tomato seeds and plants. Appl Environ Microbiol 76: 3978-3988
930 Zaman-Allah M, Vergara O, Araus JL, Tarekegne A, Magorokosho C, Zarco-Tejada PJ,
931   Hornero A, Alba AH, Das B, Craufurd P, Olsen M, Prasanna BM, Cairns J (2015)
932   Unmanned aerial platform-based multi-spectral imaging for field phenotyping of
933   maize. Plant Methods 11: 35
934 Zhao B, Dahlbeck D, Krasileva KV, Fong RW, Staskawicz BJ (2011) Computational and
935   biochemical analysis of the *Xanthomonas* effector AvrBs2 and its role in the
936   modulation of *Xanthomonas* type three effector delivery. PLOS Pathog 7:
937   e1002408
938 Zhao B, Lin X, Poland J, Trick H, Leach J, Hulbert S (2005) A maize resistance gene
939   functions against bacterial streak disease in rice. Proc Natl Acad Sci USA 102:
940   15383-15388
941

28
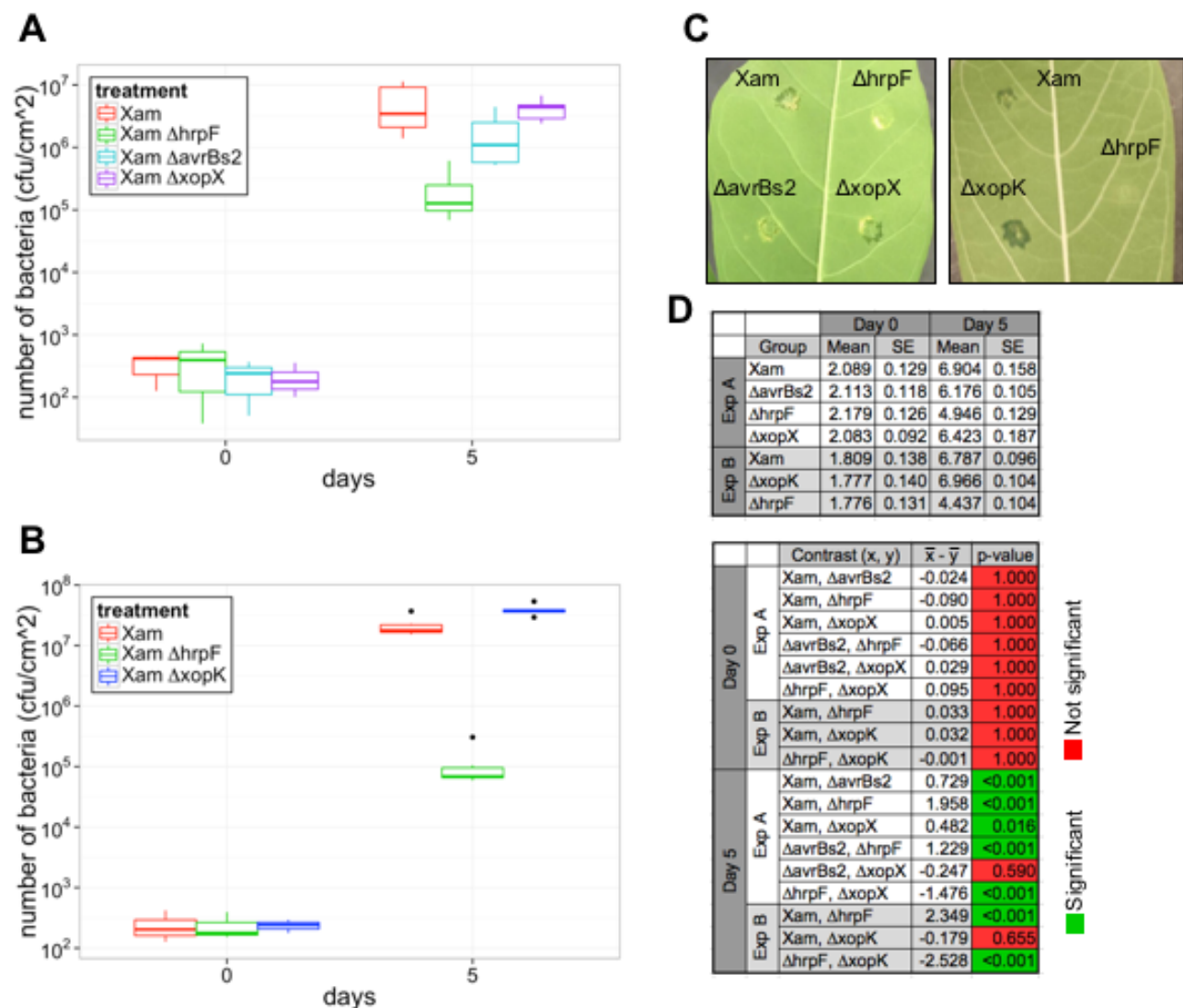
Figure 1. Disease symptom development and growth levels for *Xam* type III effector (T3E) mutants in cassava. A-B, Growth levels of *Xam* wild-type, ΔhrpF, ΔavrBs2, ΔxopX, and ΔxopK mutants following syringe infiltration in leaves (OD_{600} = 0.0001). Median, first and third quartiles are shown. The whiskers extend to the highest and lowest data point falling within 1.5*IQR (inter-quartile range). Dots represent outliers that fall outside 1.5*IQR. Each experiment was repeated three additional times (see Supplemental Fig. S1). C, Comparison of disease symptoms caused by T3E mutants on leaves at 6 days after syringe infiltration (OD_{600} = 0.0001). D, Results of generalized linear mixed model analysis, combining bacterial growth data from all replicate experiments. Combined estimated means and standard error (SE) are presented, as well as the difference between the means and p-values for each pairwise statistical contrast.
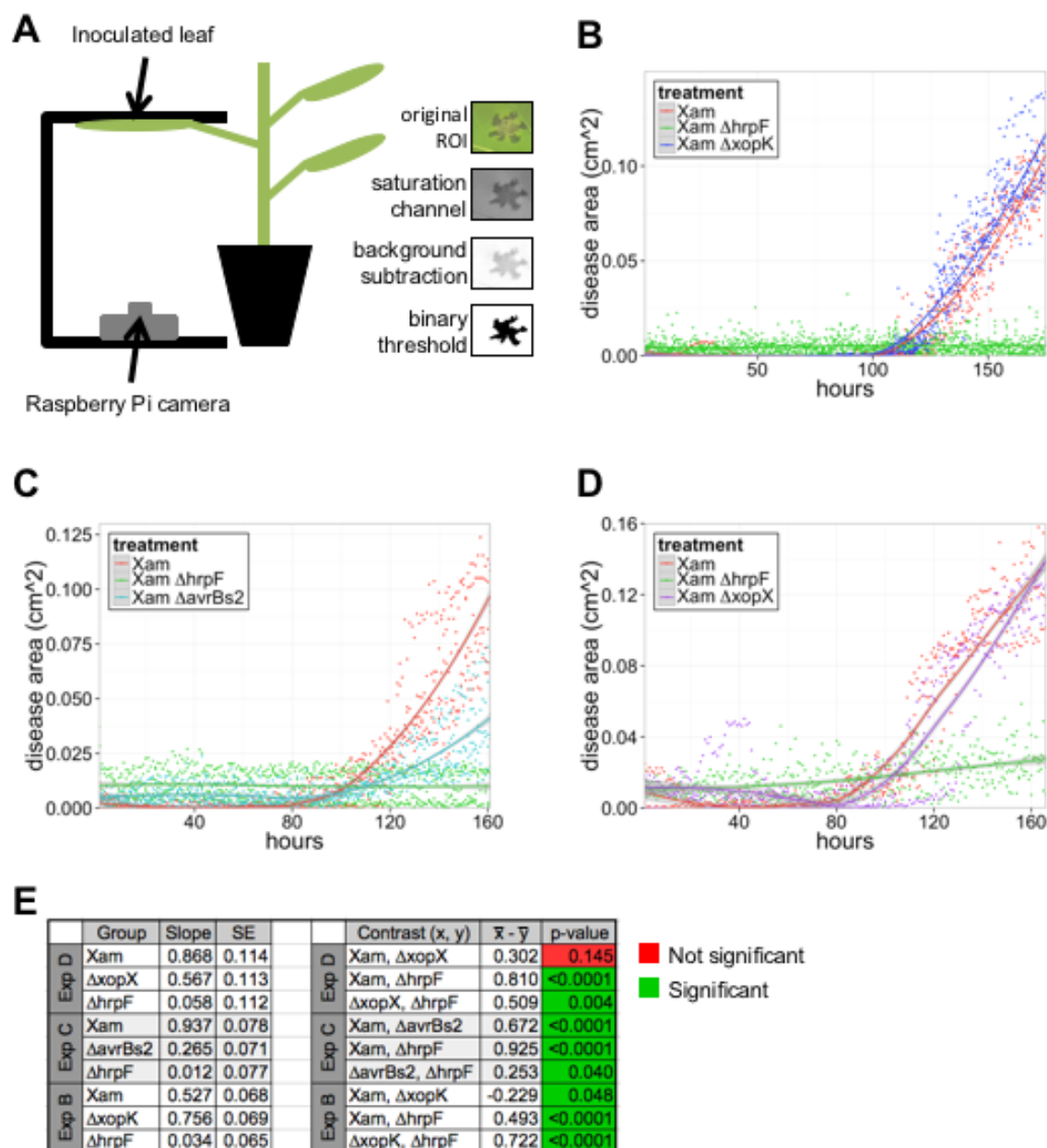
Figure 2. Quantification of disease symptoms caused by *Xam* on cassava leaves using imaging. A, Illustration of the imaging set-up. Leaves were syringe infiltrated with bacterial solutions (OD_{600} = 0.001) and taped to a black surface for imaging of the abaxial side of the leaf. Raspberry Pi microcomputer with attached camera collected images once per hour. Image analysis steps in ImageJ are shown and described in Materials and Methods. The number of black pixels was quantified to determine the area of disease. B-D, Quantification of water-soaking symptoms caused by the *Xam* wild-type strain and three mutants over time. Dots represent individual measurements determined from image analysis, and local regression fitted curves are plotted for each bacterial strain. Shaded areas represent the 95% confidence interval for each curve. The experiment was repeated three additional times with similar results (see Supplemental Fig. S3). E, Results of generalized linear mixed model analysis, combining data from all replicate experiments. Combined estimated slopes and standard error (SE) are presented, as well as p values for each pairwise statistical contrast.
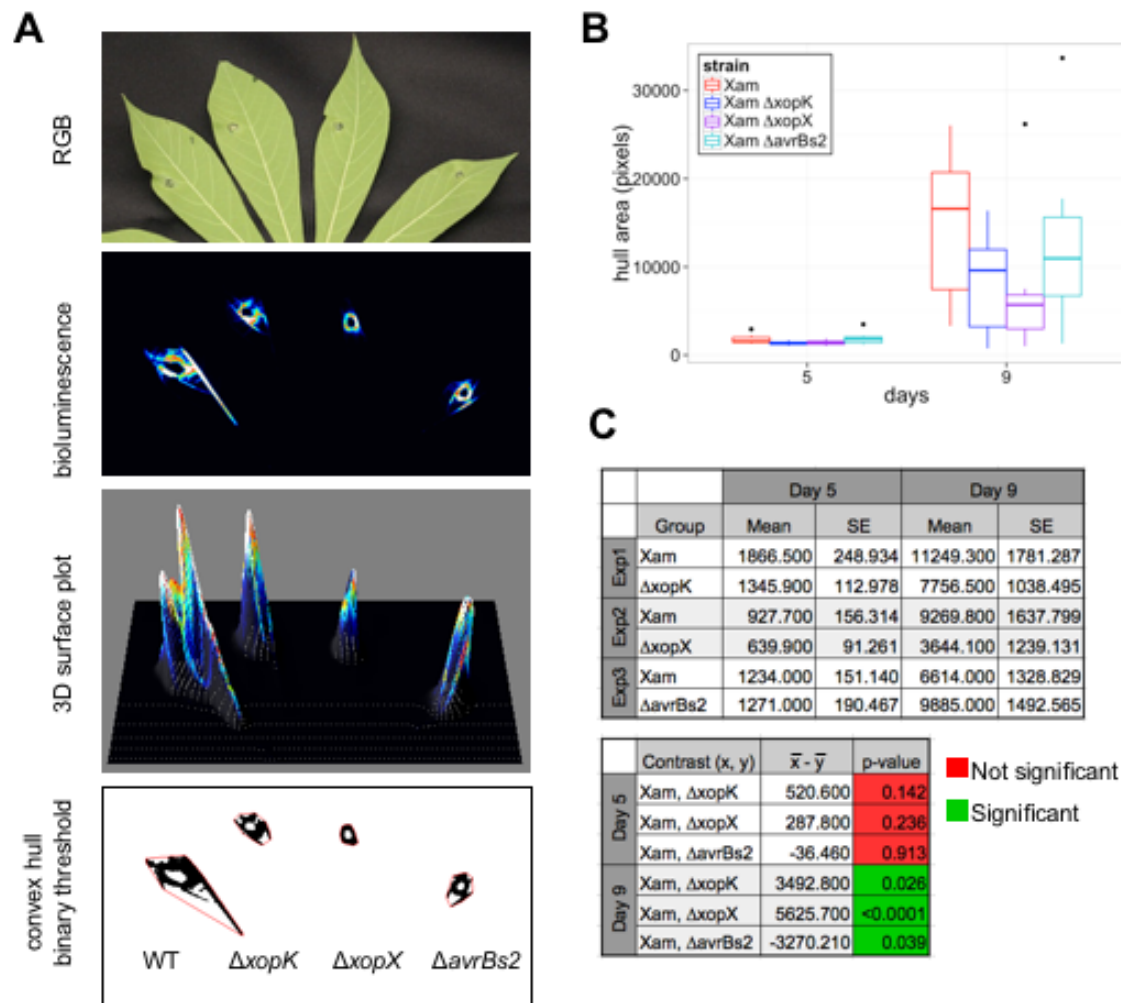
Figure 3. Bioluminescence imaging of *Xam* spread in cassava leaves. A, The bioluminescence reporter pLUX plasmid was introduced into *Xam* strains. Leaves were inoculated with bacterial solutions (OD_{600} = 0.01) using syringe infiltration. RGB images of inoculated leaves reveal symptom development. Bioluminescence was visualized in a dark chamber with a 5-10 min exposure. Image processing was performed with ImageJ to select the area of bioluminescence and the convex hull of the resulting shapes were analyzed. B, Representative quantification of convex hull for wildtype Xam and three mutants. Additional replicate experiments are shown in Supplemental Fig. S4. C, Results of generalized linear mixed model analysis of convex hull area, combining data from all replicate experiments. Combined estimated means and standard error (SE) are presented, as well as the difference between the means and the p-values for each pairwise statistical contrast.
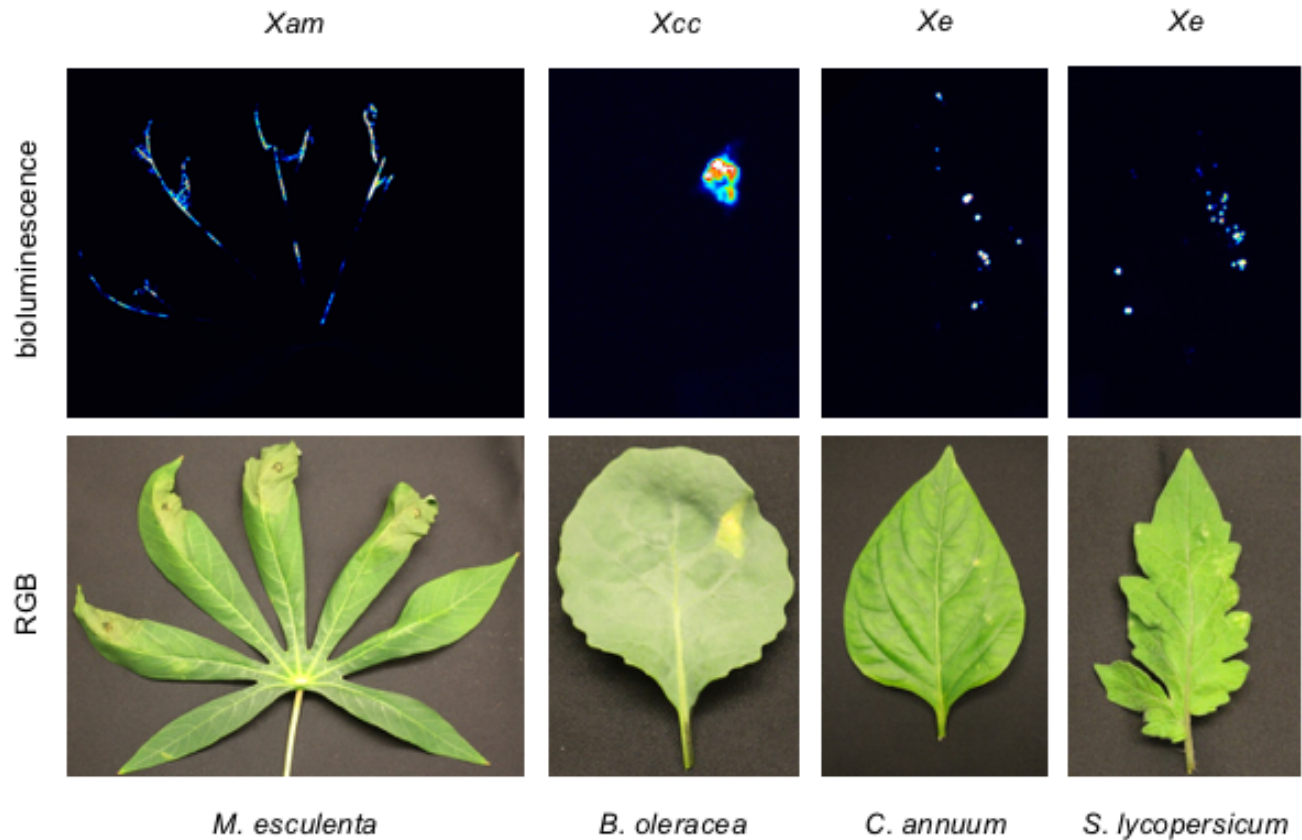
Figure 4. Comparison of vascular and leaf spot pathogens. *Xam* and *Xcc* were visualized following syringe inoculation (OD_{600} = 0.01) at 18 days post inoculation (dpi) and 12 dpi, respectively. Bacterial spot on pepper and tomato were visualized following dip inoculation (OD_{600} = 0.5) of *Xe* at 9 dpi.
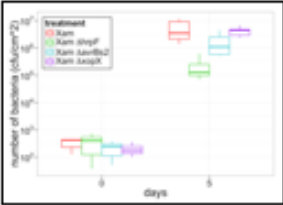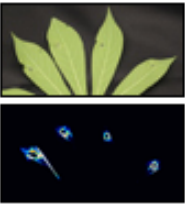
| Xam T3E mutant	Growth levels *in planta*	Disease symptom progression	Bacterial spread *in planta*	*In vitro* motility
ΔxopK	No change	Increased	Decreased	No change
ΔxopX	Decreased	No change	Decreased	No change
ΔavrBs2	Decreased	Decreased	Decreased	No change

Figure 5. Summary for T3E mutant phenotypes as revealed by different phenotyping methods.
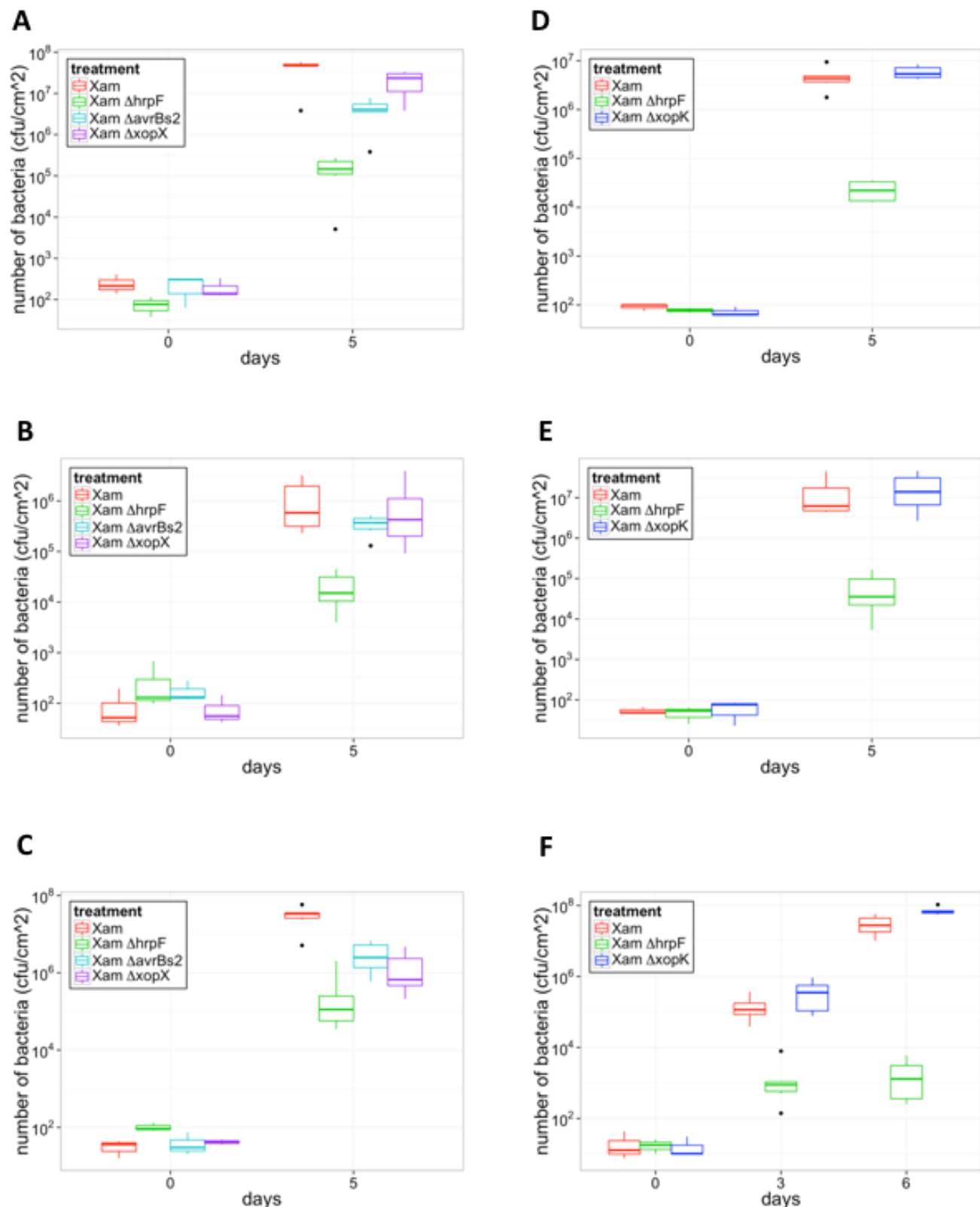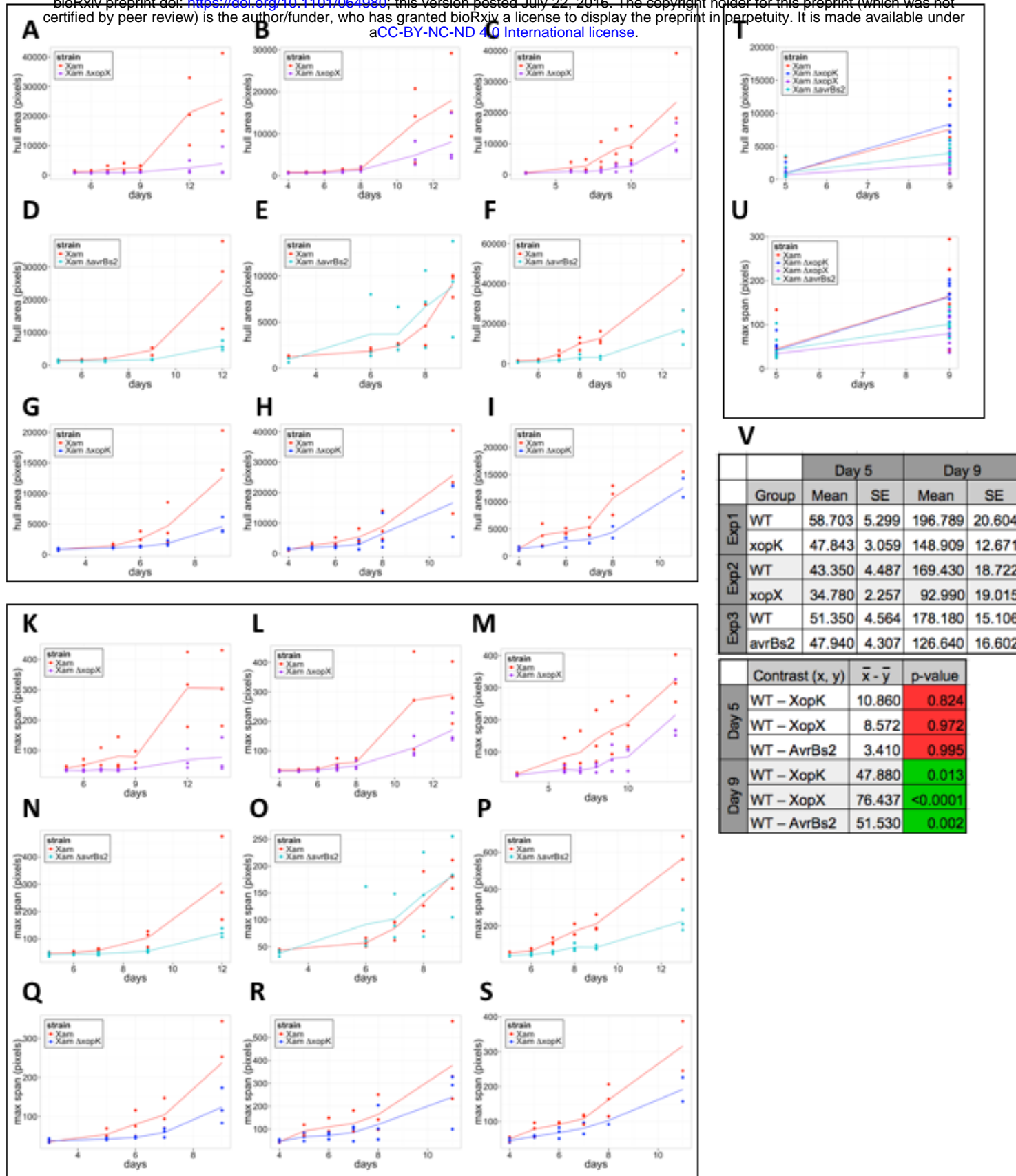
Supplemental Figure S1. Replicate experiments for analysis of *Xam* T3E mutant growth *in planta* shown in Figure 1. A-C, Three additional experiments to quantify growth levels of the *Xam* wild type strain, and the *Xam ΔhrpF*, *ΔavrBs2*, and *ΔxopX* mutants following syringe infiltration in leaves (OD$_{600}$ = 0.0001). D-F, Three additional experiments to quantify growth levels of wild-type *Xam*, and the *ΔhrpF* and *ΔxopK* mutants following syringe infiltration in leaves (OD$_{600}$ = 0.0001).
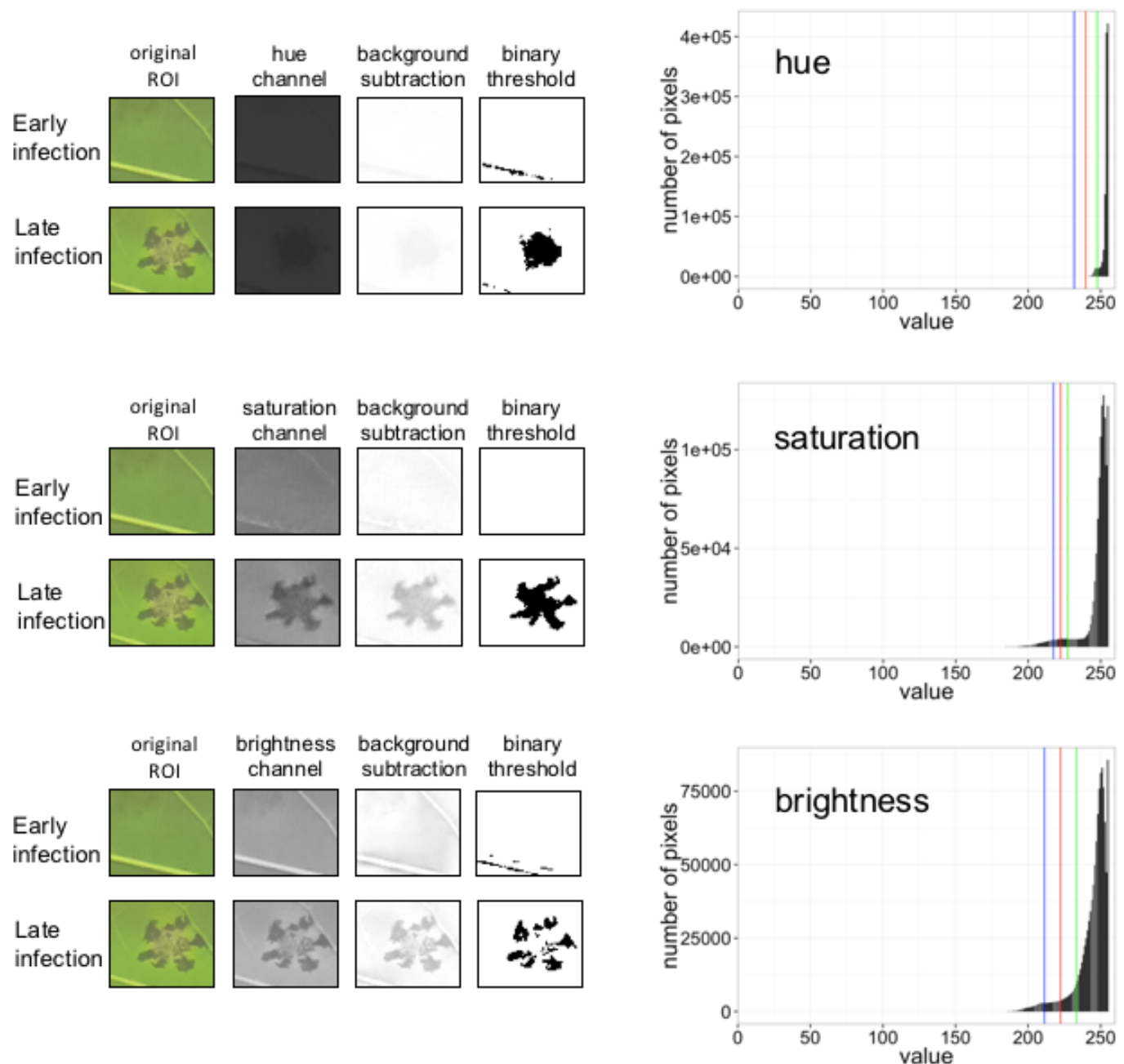
Supplemental Figure S2. Image analysis optimization for water-soaking disease symptoms caused by *Xam*. Following conversion of regions of interest (ROI) to hue-saturation-brightness (HSB) color space and background subtraction, the distributions of pixel values for each channel were examined. Disease symptoms are best represented by pixel values in the lower tail of the distribution for the saturation channel. A range of threshold values were applied to the images to create binary images, according to the formula $t = \mu - n\sigma$, where t = threshold, μ = mean saturation value for the image stack, and σ = standard deviation of saturation values for the image stack. Graphs show example thresholds where $n = 3$ (blue line), $n = 2.5$ (red line), and $n = 2$ (green line). The binary images on the right show the results of applying the $n = 3$ threshold.
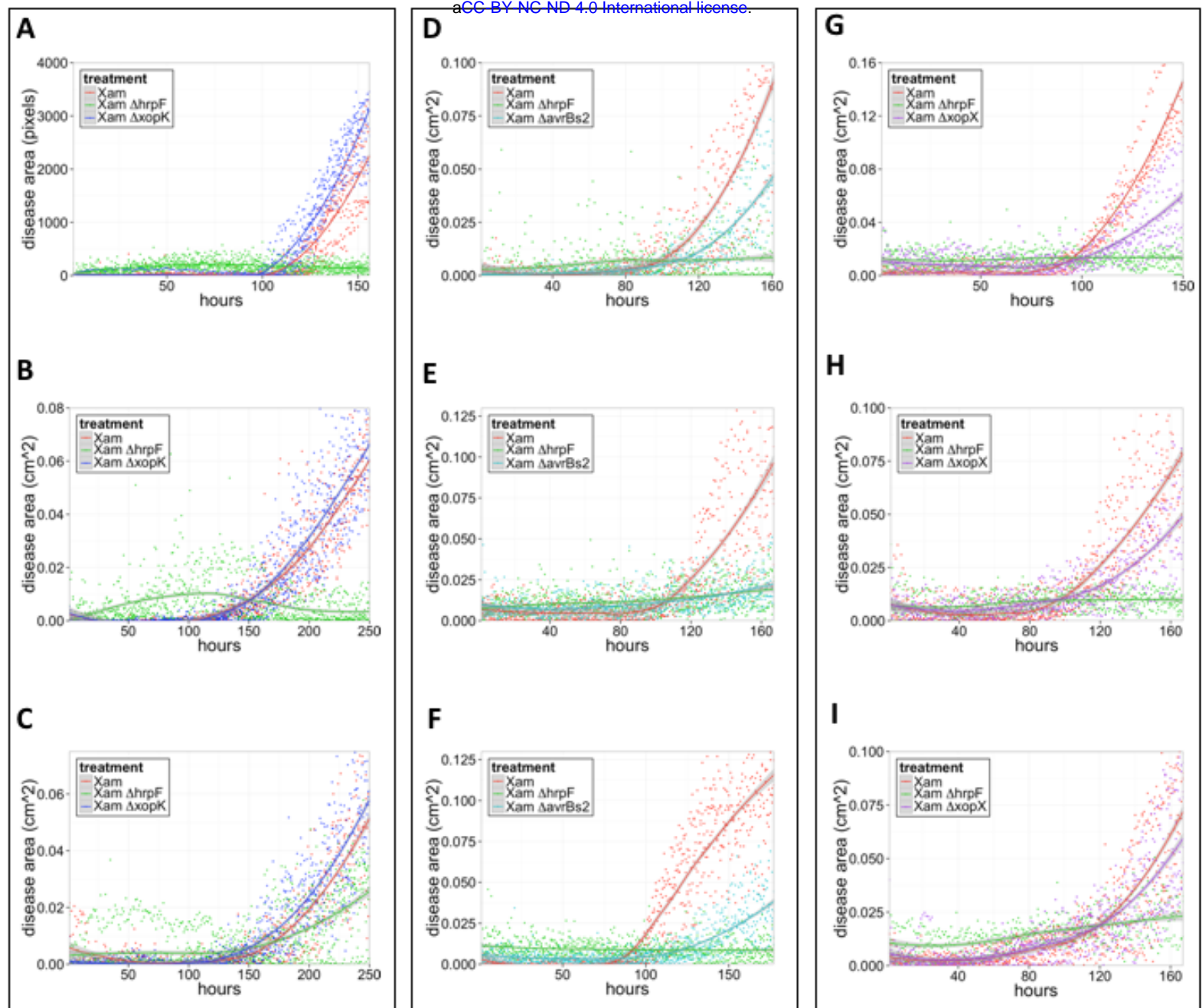
Supplemental Figure S3. Three additional replicate experiments for analysis of water-soaking symptoms shown in Fig. 2. Dots represent individual measurements determined from image analysis, and local regression fitted curves are plotted for each bacterial strain. Shaded areas represent the 95% confidence interval for each curve. For the experiment shown in A, the image distances were not scaled to cm, so values are reported in pixels. Experiments shown in panels D-F and H-I were performed with cassava variety TME7.

Supplemental Figure S4. Replicate experiments for analysis of *Xam* spread in leaves using bioluminescence imaging shown in Fig. 3. Three additional experiments quantifying the convex hull area for the *Xam ΔxopX* (A-C), *ΔavrBs2* (D-F), and *ΔxopK* (G-I) mutants. Quantification of the maximum span across the convex hull for the same experiments (K-S). Quantification of the convex hull area (T) and maximum span (U) for a fourth replicate experiment including the three mutants. Dots represent individual measurements; lines connect the mean at each time point. V, Results of generalized linear mixed model analysis for maximum span results, combining data from all replicate experiments. Combined estimated means and standard error (SE) are presented, as well as p values for each pairwise statistical contrast.
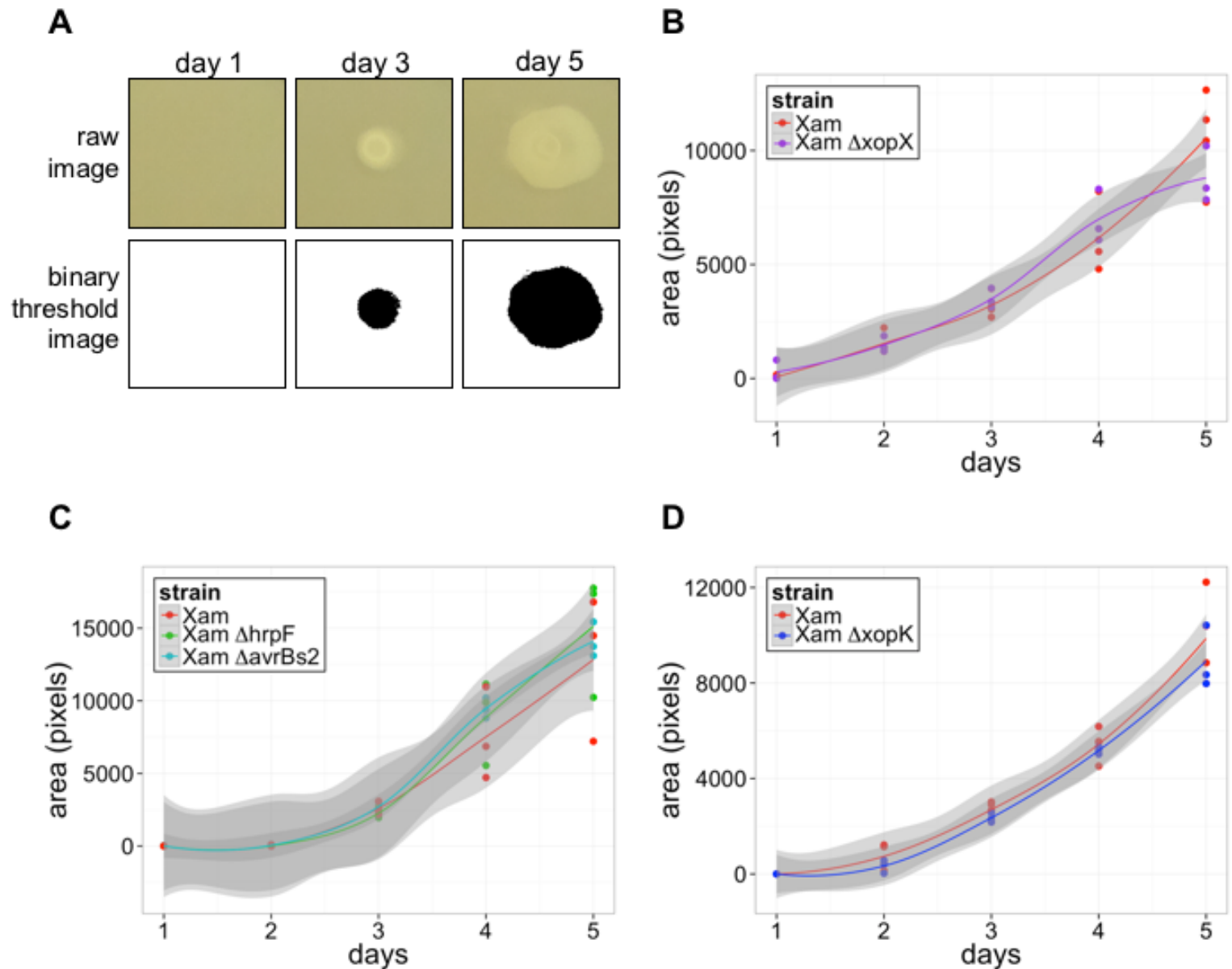
Supplemental Figure S5. *In vitro* motility of *Xam* T3E mutants. Bacteria were spotted in the center of plates containing NYG media with 0.25% agar. Images were taken of the plates over several days, and the area of bacterial spread was quantified using ImageJ. A, Example of binary thresholding used to select the area of bacterial spread from the images. B-D, Quantification of bacterial spread for the *Xam* T3E mutants, relative to the wild-type strain. Dots represent individual data points, and local regression fitted curves are plotted for each bacterial strain. Shaded areas represent the 95% confidence interval for each strain.

```
/***********************************************************************
 * Author: Andrew Mutka, Donald Danforth Plant Science Center, St. Louis, MO
 *
 * ImageJ macro script to select and quantify the area of water-soaking disease
 * symptoms for regions of interest from images of inoculated leaves
 *
 ***********************************************************************/

function ws_quant(input, output, filename) {
        open(input + filename);
        sourceTitle = getTitle();
        selectWindow(""+sourceTitle+"");
        //convert images to HSB color space and select the saturation channel
        run("HSB Stack");
        run("Split Channels");
        selectWindow("C1-"+sourceTitle+"");
        close;
        selectWindow("C3-"+sourceTitle+"");
        close;
        selectWindow("C2-"+sourceTitle+"");
        //subtract background from the images
        run("Subtract Background...", "rolling=50 light stack");
        //calculate the mean and standard deviation of saturation values from the image stack
        run("Set Measurements...", "mean standard redirect=C2-"+sourceTitle+" decimal=9");
        run("Statistics");
        selectWindow("Results");
        mean=getResult("Mean");
        stdDev=getResult("StdDev");
        //set n as a multiple of stdDev to calculate the desired threshold level
        n=3;
        threshold=mean-(n*stdDev);
        //print a log of threshold values used
        print(mean, stdDev, threshold);
        //apply the threshold to the image stack
        selectWindow("C2-"+sourceTitle+"");
        setAutoThreshold("Default");
        setThreshold(0, threshold);
        run("Convert to Mask", "method=Default background=Default");
        //save the binary images
        saveAs("Tiff", output + filename);
        //calculate the area of black pixels in the binary images
        run("Set Measurements...", "area redirect=["+sourceTitle+"] decimal=9");
        run("Analyze Particles...", "summarize stack");
        //save the results as a csv file
        saveAs("Results", output + filename + ".csv");
        close();
        run("Clear Results");
}

//set input/output variables based on directory containing images and desired output directory
input = "/Users/amutka/input/";
output = "/Users/amutka/output/";

//calculate threshold areas for each image stack in a directory
setBatchMode(true);
list = getFileList(input);
for (i = 0; i < list.length; i++)
        ws_quant(input, output, list[i]);
setBatchMode(false);
```

```
/*****************************************************************************
 * Author: Andrew Mutka, Donald Danforth Plant Science Center, St. Louis, MO
 *
 * ImageJ macro script to quantify bacterial spread on soft agar plates
 *
 *****************************************************************************/

function motility_quant(input, output, filename) {
        open(input + filename);
        sourceTitle = getTitle();
        selectWindow(""+sourceTitle+"");
        //convert to 8-bit grayscale images
        run("8-bit");
        //enhance contrast of the images
        run("Enhance Contrast...", "saturated=0.4 normalize process_all use");
        //create binary images using thresholding
        run("Auto Threshold", "method=MaxEntropy white stack use_stack_histogram");
        run("Despeckle", "stack");
        run("Invert", "stack");
        run("Convert to Mask", "stack");
        //save the binary images
        saveAs("Tiff", output + filename);
        //calculate the area of black pixels in the binary images
        run("Set Measurements...", "area redirect=["+sourceTitle+"] decimal=9");
        run("Analyze Particles...", "include summarize stack");
        //save the results as a csv file
        saveAs("Results", output + filename + ".csv");
        close();
}

//set input/output variables based on directory containing images and desired output directory
input = "/Users/amutka/input/";
output = "/Users/amutka/output/";

//calculate threshold area for each image stack in the directory
setBatchMode(true);
list = getFileList(input);
for (i = 0; i < list.length; i++)
        motility_quant(input, output, list[i]);
setBatchMode(false);
```